

Hales CA, Murphy T, Curran JR, Middelberg E, Gaensler BM, Norris RP.  
[BLOBCAT: software to catalogue flood-filled blobs in radio images of total intensity and linear polarization.](#)

*Monthly Notices of the Royal Astronomical Society* 2012, 425(2), 979-996.

**Copyright:**

This article has been accepted for publication in *Monthly Notices of the Royal Astronomical Society* © 2012 The Authors. Published by Oxford University Press on behalf of the Royal Astronomical Society. All rights reserved.

**DOI link to article:**

<https://doi.org/10.1111/j.1365-2966.2012.21373.x>

**Date deposited:**

30/06/2017

# BLOBCAT: software to catalogue flood-filled blobs in radio images of total intensity and linear polarization

C. A. Hales,<sup>1,2\*</sup> T. Murphy,<sup>1,3,4</sup> J. R. Curran,<sup>3</sup> E. Middelberg,<sup>5</sup> B. M. Gaensler<sup>1,4</sup>  
and R. P. Norris<sup>2,4</sup>

<sup>1</sup>*Sydney Institute for Astronomy, School of Physics, The University of Sydney, NSW 2006, Australia*

<sup>2</sup>*CSIRO Astronomy & Space Science, PO Box 76, Epping, NSW 1710, Australia*

<sup>3</sup>*School of Information Technologies, The University of Sydney, NSW 2006, Australia*

<sup>4</sup>*ARC Centre of Excellence for All-sky Astrophysics (CAASTRO), The University of Sydney, NSW, 2006 Australia*

<sup>5</sup>*Astronomisches Institut, Ruhr-Universität Bochum, Universitätsstr. 150, 44801 Bochum, Germany*

Accepted 2012 May 23. Received 2012 May 22; in original form 2011 October 7

## ABSTRACT

We present BLOBCAT, new source extraction software that utilizes the flood fill algorithm to detect and catalogue blobs, or islands of pixels representing sources, in 2D astronomical images. The software is designed to process radio-wavelength images of both Stokes  $I$  intensity and linear polarization, the latter formed through the quadrature sum of Stokes  $Q$  and  $U$  intensities or as a by-product of rotation measure synthesis. We discuss an objective, automated method by which estimates of position-dependent background root mean square noise may be obtained and incorporated into BLOBCAT's analysis. We derive and implement within BLOBCAT corrections for two systematic biases to enable the flood fill algorithm to accurately measure flux densities for Gaussian sources. We discuss the treatment of non-Gaussian sources in light of these corrections. We perform simulations to validate the flux density and positional measurement performance of BLOBCAT, and we benchmark the results against those of a standard Gaussian fitting task. We demonstrate that BLOBCAT exhibits accurate measurement performance in total intensity and, in particular, linear polarization. BLOBCAT is particularly suited to the analysis of large survey data.

**Key words:** methods: data analysis – methods: statistical – techniques: image processing – techniques: polarimetric – catalogues – surveys.

## 1 INTRODUCTION

In radio astronomy image analysis, for which approximations of Gaussian noise statistics and Gaussian source morphologies are suitable, much attention has been paid to least-squares 2D elliptical Gaussian fitting routines (e.g. Condon 1997). Such routines, for example those implemented within the MIRAID (Sault, Teuben & Wright 1995) and AIPS (Bridle & Greisen 1994) packages, are appropriate for source extraction when fitting parameters have been carefully inspected or constrained. However, when left unconstrained, the accuracy of these Gaussian fits may become degraded, requiring significant manual inspection overheads to identify poor fits and ensure high-quality source extraction. Gaussian fitting routines may therefore be unsuited to the general analysis of large survey data.

In this work, we seek to develop a robust alternative to Gaussian fitting by utilizing the flood fill algorithm (Lieberman 1978; Fishkin & Barsky 1985). In particular, we seek to develop a source extraction procedure that incorporates an accurate, objective and automated

method of background root mean square (rms) noise estimation, and to develop the first accurate method of source extraction for resolved sources in linear polarization. Additional factors motivating this work are described as follows.

First, a number of large radio surveys are planned for the near future, capitalizing on upcoming new or substantially upgraded facilities such as ASKAP (Johnston et al. 2008; Deboer et al. 2009), MEERKAT (Jonas 2009), LOFAR (Rottgering et al. 2010), ALMA (Wootten & Thompson 2009; Hills, Kurz & Peck 2010), LWA (Ellingson et al. 2009), WSRT (Oosterloo et al. 2009), EVLA (Perley et al. 2011) and many others including very long baseline interferometry networks and epoch of reionization instruments. With these facilities will come a number of large surveys in both total intensity and linear polarization, for example EMU (Norris et al. 2011), WODAN,<sup>1</sup> MIGHTEE,<sup>2</sup> POSSUM (Gaensler et al. 2010) and GALFACTS (Taylor & Salter 2010). The ability to catalogue

<sup>1</sup> <http://www.astron.nl/radio-observatory/apertif-eoi-abstracts-and-contact-information>

<sup>2</sup> Van der Heyden K., Jarvis M. J., 2010, MIGHTEE proposal to MEERKAT.

\*E-mail: c.hales@physics.usyd.edu.au

objects within the large images produced by these surveys, with as little manual intervention as possible, will be key to maximizing scientific output. We seek to develop a robust, automated method of source extraction that requires only the most complex sources to be manually inspected.

Secondly, recent polarimetric studies have indicated an increase in the fractional polarization of faint extragalactic radio sources (e.g. Taylor et al. 2007; Grant et al. 2010; Shi et al. 2010; Subrahmanyan et al. 2010), which are difficult to reconcile with population modelling (O’Sullivan et al. 2008). We seek here to subject the process of polarization measurement to close scrutiny, and to provide the community with a measurement tool that has been assessed within a controlled testing environment.

Thirdly, the flood fill algorithm underpins a number of existing source extraction routines, such as those available in the CUPID<sup>3</sup> (e.g. CLUMPFIND; Williams, de Geus & Blitz 1994) and SExtractor (Bertin & Arnouts 1996) packages. However, these routines are unable to measure flux densities without performing subsequent Gaussian (or similar) source fitting. Alternatively, the flood fill algorithm has been used without the subsequent least-squares fitting step for the customized analysis of extended, non-Gaussian sources in total intensity (Murphy et al. 2007) and linear polarization (Heald, Braun & Edmonds 2009). However, the raw flood fill algorithm as implemented in these works is not suitable for use with compact (unresolved or resolved Gaussian) sources, as their flux density measurements suffer from two significant systematic biases. In this work we describe how to correct for these biases in a robust manner, so as to enable the flood fill approach to handle both Gaussian and non-Gaussian sources.

We have implemented these bias corrections within a new flood fill program called BLOBCAT, which catalogues blobs in astronomical images. We use the term *blob* in an image-processing sense to represent an island of agglomerated pixels within a sea of noise, and to indicate that its properties are not inferred by fitting (e.g. least squares). We have designed BLOBCAT for use in radio astronomy, attempting to produce a program capable of encapsulating the entire measurement process between observational image and output catalogue.

This paper is organized as follows. In Section 2, we describe the algorithms implemented within BLOBCAT, detailing required program inputs, including the minimal set required for operation and output data products. In Section 3, we assess BLOBCAT’s peak surface brightness (SB), integrated SB and positional measurement performance. We investigate the program’s ability to handle unresolved, resolved and complex (non-Gaussian) sources in images of total intensity (Stokes  $I$ ) and linear polarization ( $L$  or  $L_{RM}$ ; these terms are defined in Section 2) and discuss issues regarding polarization bias. For comparison, we also assess the performance of a standard Gaussian fitting routine. In Section 4, we discuss two examples of post-processing that may be required to make full use of BLOBCAT’s output catalogue; these are particularly relevant for data containing extended non-Gaussian, or multiple blended Gaussian, sources. In Section 5, we present our summary and conclusions.

## 2 HOW BLOBCAT WORKS?

BLOBCAT is written in the scripting language PYTHON. The program is designed to catalogue blobs in a 2D input FITS (Pence et al. 2010) image of SB. To isolate blobs and determine their properties,

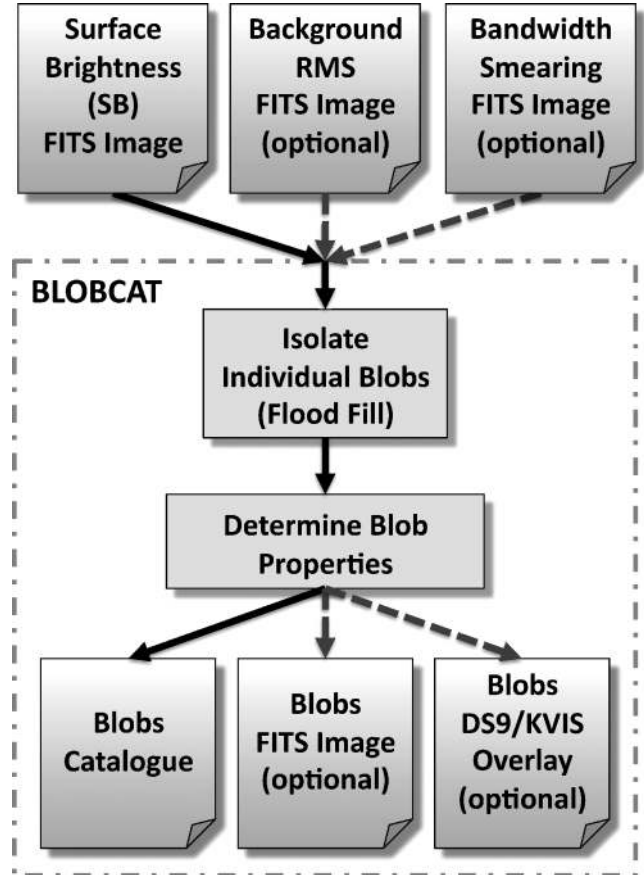


Figure 1. Overview of BLOBCAT.

BLOBCAT requires an estimate of the background rms noise and degree of bandwidth smearing at each spatial position (pixel) within the SB image. These two diagnostics may be provided to BLOBCAT as either uniform (spatially invariant) values or, more generally, as 2D input FITS images that encode the more realistic scenario whereby noise and smearing properties vary with spatial position over the SB image.

An overview of BLOBCAT is presented in Fig. 1. In the following sections, we describe the input images and their requirements (Section 2.1), the core flood fill algorithm used to isolate blobs (Section 2.2), the key morphological assumption (Section 2.3) and bias corrections (Section 2.4) applied to extract blob properties, the input arguments required to run BLOBCAT (Section 2.5), the output catalogue (Section 2.6) and the optional program outputs (Section 2.7).

### 2.1 Input images

BLOBCAT requires up to three input FITS images, as outlined in Fig. 1. For flexibility, the images of background rms noise and bandwidth smearing are optional, and may instead be replaced by spatially invariant input values.

#### 2.1.1 Surface brightness

BLOBCAT is designed to analyse blobs with positive SB. To detect negative blobs, the input SB image must be inverted before use. In this paper, we focus on the analysis of blobs in images of total intensity and linear polarization ( $L$  or  $L_{RM}$ ). BLOBCAT may also be

<sup>3</sup> <http://starlink.jach.hawaii.edu/starlink/CUPID>

used to analyse images of Stokes  $Q$ ,  $U$  and  $V$  intensities, though we note that resolved sources exhibiting both positive and negative SB in these images will be incorrectly handled; we do not attempt to address the analysis of such sources here. We assume that blobs of interest in total intensity and linear polarization may be characterized by 2D elliptical Gaussians, though we do consider the treatment of non-Gaussian blobs later in Section 4.2. Image pre-processing techniques to remove widespread extended features prior to the analysis of more compact sources may be required (e.g. Rudnick 2002; Rudnick & Brown 2009; Oppermann, Robbers & Ensslin 2011).

We assume that images of  $L_{\text{RM}}$  are produced following the application of rotation measure (RM) synthesis (Brentjens & de Bruyn 2005) and  $\text{RM}_{\text{CLEAN}}$  (Heald et al. 2009) such that for each spatial pixel located at pixel coordinate  $(x, y)$ , the polarized emission is obtained by taking the peak value in the cleaned Faraday dispersion function, namely

$$L_{\text{RM}}(x, y) = \max(|F^{\text{cleaned}}(x, y, \phi)|), \quad (1)$$

where  $\phi$  is the Faraday depth. We note that this definition of  $L_{\text{RM}}$  assumes Faraday spectra along each pixel sightline consisting of no more than a single unresolved Faraday component (additional components will be ignored); analysis with more advanced models of  $L_{\text{RM}}$  is beyond the scope of this work. Analysis involving equation (1) is demonstrated, for example, by Heald et al. (2009) and Hales et al. (in preparation). Alternatively, images of standard linear polarization,

$$L(x, y) = \sqrt{Q(x, y)^2 + U(x, y)^2}, \quad (2)$$

may be used. See Leahy & Fernini (1989) and Vaillancourt (2006) for statistical properties of  $L$ , and Hales et al. (2012) for statistical properties of both  $L$  and  $L_{\text{RM}}$ . For simplicity in subsequent discussion, we neglect the pixel coordinate notation  $(x, y)$  affixed to all spatially variable parameters, unless required for clarity.

### 2.1.2 Background rms noise

If position-dependent rather than spatially invariant blob detection thresholds are required, then a background rms noise image must be specified. The user is required to independently construct a suitable noise map for the SB image, for example using the rms estimation algorithm implemented within the  $\text{SE}_{\text{EXTRACTOR}}$  package (Bertin & Arnouts 1996; Holwerda 2005).

Despite having been originally developed for the analysis of optical photographic plate and CCD data,  $\text{SE}_{\text{EXTRACTOR}}$  has been found to be reliable when generating noise maps from radio data (Bondi et al. 2003; Huynh et al. 2005).  $\text{SE}_{\text{EXTRACTOR}}$  determines the rms noise at each spatial pixel in an image by extracting the distribution of pixel values within a local mesh, iteratively clipping the most deviant values until convergence is reached at  $\pm 3\sigma$  about the median. The choice of mesh size (in  $\text{pixel}^2$ ) is very important. If it is too small, the local rms estimate may be biased due to the lack of statistically independent measurements or overestimated due to the presence of real sources. If it is too large, any true small-scale variations in local rms noise may be washed out. At least  $N_b = 80$  independent resolution elements (beams) per mesh area are required in order to reduce the uncertainty in estimates of local rms noise to below  $\{[1 + 0.75/(N_b - 1)]^2 [1 - N_b^{-1}] - 1\}^{0.5} = 8$  per cent (using an approximation to the uncertainty of the standard error estimator, suitable for  $N_b > 10$ ; Johnson & Kotz 1970, p. 63). The mesh area,

$H_{\text{mesh}}$ , may be calculated according to

$$H_{\text{mesh}} = \frac{N_b}{\bar{d}} \Omega_b, \quad (3)$$

where

$$\Omega_b = \frac{\pi}{4 \ln 2} \Theta_{\text{maj}} \Theta_{\text{min}} \quad (4)$$

is the beam volume for a 2D elliptical Gaussian with full width at half-maximum (FWHM) along the major and minor axes given by  $\Theta_{\text{maj}}$  and  $\Theta_{\text{min}}$ , respectively, and where  $\bar{d} = \pi/\sqrt{12}$  is the densest lattice packing for congruent copies of any convex shape (e.g. circles, ellipses; Pach & Agarwal 1995). It is customary in physical sciences to treat rms noise<sup>4</sup> values, such as those reported by  $\text{SE}_{\text{EXTRACTOR}}$ , as standard errors in order to boost noise estimates in regions where extended non-signal features are present, namely by defining that  $\sigma_z = (z_{\text{rms}})_{\text{SE}_{\text{EXTRACTOR}}}$ . In other words, by using rms noise estimates to calculate local signal-to-noise ratio (S/N) thresholds for blob detection, it is possible to take into account not only local variations in image sensitivity, but also the possible presence of DC offsets due to artefacts (e.g. sidelobes). For this reason, we recommend the method of using  $\text{SE}_{\text{EXTRACTOR}}$  or a similar package to estimate noise over the method of simply estimating it from, say, Stokes  $V$  because it can take into account features in the data that may be missed by more theoretically motivated expectations. The procedure described above, incorporating equation (3), may be easily automated to provide objective estimates of rms noise for any noise-dominated image.

Finally, we note that the  $\text{SE}_{\text{EXTRACTOR}}$  procedure above is suitable for determining the rms noise in images of Stokes  $I$ ,  $Q$ ,  $U$  or  $V$ , but not  $L_{\text{RM}}$  (nor  $L$ ). Instead, to determine  $\sigma_{\text{RM}}$  at each spatial location in  $L_{\text{RM}}$ ,  $\text{SE}_{\text{EXTRACTOR}}$  should be run on each constituent  $Q_i$  and  $U_i$  image in each  $i$ th of  $T$  frequency channels to obtain  $\sigma_{Q,i}$  and  $\sigma_{U,i}$ . These in turn may then be combined using weighted least squares as (Hales et al. 2012)

$$\sigma_{\text{RM}} = \left[ \xi \sum_{i=1}^T \frac{1}{0.2 \min(\sigma_{Q,i}^2, \sigma_{U,i}^2) + 0.8 \max(\sigma_{Q,i}^2, \sigma_{U,i}^2)} \right]^{-1/2}, \quad (5)$$

where the term  $\xi$  represents the correlation correction factor defined by equation (23) from Hales et al. (2012).

### 2.1.3 Bandwidth smearing

If corrections for position-dependent bandwidth smearing (chromatic aberration) are required, then an image detailing the degree of smearing at any location within the SB image must be specified. Bandwidth smearing is due to the finite bandwidth of frequency channels, resulting in a radially dependent convolution (smearing) that worsens as a function of positional offset from the phase tracking centre of a single-pointed radio observation (Condon et al. 1998; Bridle & Schwab 1999). The effect is to decrease the peak SB and to increase the observed size of sources without affecting their integrated SB. Bandwidth smearing needs to be carefully accounted for in mosaics consisting of multiple overlapped pointings. This is because any location in a mosaicked image, even one situated over a pointing centre, may include multiple contributions from adjacent pointings in which bandwidth smearing is significant (Ibar et al. 2009). The bandwidth smearing image input to  $\text{BLOBCAT}$  should map out the ratio between the observed smeared peak SB,  $S_p$ , and

<sup>4</sup> The definition of rms noise is  $z_{\text{rms}}^2 = \bar{z}^2 + \sigma_z^2$ .

the true unsmeared peak SB,  $S_p^{\text{BWS}}$ , for all spatial positions within the SB image (using notation consistent with that introduced later in this work). We denote the local degree of bandwidth smearing as

$$\varpi = \frac{S_p}{S_p^{\text{BWS}}} (\leq 1). \quad (6)$$

### 2.1.4 General requirements

All images input to `BLOBCAT` must have the same dimensions and be located on the same pixel grid; for cataloguing purposes, we require that the primary image world coordinate system is expressed in equatorial coordinates (RA–Dec.). In order to measure fitted Gaussian peaks to within 1 per cent, at least 5 pixel per resolution element FWHM should be present (see Appendix A).

`BLOBCAT` does not calculate the Jacobian of the transformation between projection plane coordinates and native longitude and latitude (Calabretta & Greisen 2002). Instead, `BLOBCAT` requires that input images are gridded to an equal-area projection, so as to ensure that sky area per pixel is preserved. `BLOBCAT` supports both zenithal equal-area (ZEA) projection (the premier scheme for a hemisphere) and Hammer–Aitoff (AIT) equal-area projection (suitable for all-sky images) (Calabretta & Greisen 2002). Failure to use an equal-area projection will lead to systematic biases in `BLOBCAT`’s extracted flux densities and visibility area (sky density) calculations (see Section 2.6). However, there are two common situations where this equal-area requirement may be relaxed. The first is when measuring flux densities for unresolved sources by obtaining their peak pixel or fitted peak value (cf. Appendix A). The second involves the use of images with non-equal-area projections; for example, the north-celestial-pole (NCP) projection (Greisen 1983). For such images, flux density measurements for resolved sources, which require integration over SB (i.e. over pixels), will only be suitable for sources situated close to the image reference point where distortion effects are minimal (Calabretta & Greisen 2002). To enable such analysis, `BLOBCAT` also supports images in NCP projection or the more general slant orthographic (SIN) projection. Re-gridding of input images to one of the ZEA, AIT, NCP or SIN projection schemes may be computed using, for example, the `WCSSLIB`<sup>5</sup> package. Finally, we remark that equal-area projections do not preserve shape; it is not possible to conserve both angles and areas when mapping portions of a sphere to a plane.

## 2.2 Flood fill algorithm

`BLOBCAT` uses the flood fill, or thresholding, algorithm (Lieberman 1978; Fishkin & Barsky 1985; Sonka, Hlavac & Boyle 2008) to isolate individual blobs (islands) of pixels from within an S/N map. The S/N map is formed by taking the pixel-by-pixel ratio between the input SB and background rms noise images. In units of dimensionless S/N, we denote the threshold for detecting blobs as  $T_d$  and the cut-off threshold for flooding down to as  $T_f$ . By applying thresholds in the S/N map rather than the SB image, local variations in sensitivity can be accommodated. We do not take into account bandwidth smearing at this initial flooding stage (see Section 2.6). We have implemented the highly optimized flood fill algorithm from Murphy et al. (2007) within `BLOBCAT`, which operates as follows.

(i) Locate all pixels in the S/N map that have value  $\geq T_d$ , including those pixels that would meet this detection threshold if they were not for pixellation attenuation (see Appendix A and comments below).

(ii) Form blobs about each of these pixels by ‘flooding’ adjacent pixels that have value  $\geq T_f$ .

(iii) For each isolated blob, perform bias corrections (Section 2.4) and catalogue properties (Section 2.6).

We denote the peak SB observed within the peak pixel for each blob by  $S_p^{\text{OBS}}$  (with units Jy beam<sup>-1</sup>), and the resulting observed peak S/N by  $A^{\text{OBS}} = S_p^{\text{OBS}}/\sigma$ . To minimize the attenuating effect of pixellation on  $S_p^{\text{OBS}}$ , `BLOBCAT` calculates a fitted peak SB for each blob by applying a 2D parabolic fit to a  $3 \times 3$  pixel array about the raw peak, as described in Appendix A. We denote this fitted peak by  $S_p^{\text{FIT}}$ , and the resulting fitted peak S/N by  $A^{\text{FIT}} = S_p^{\text{FIT}}/\sigma$ . We denote measurements of integrated SB by  $S_{\text{int}}^{\text{OBS}}$  (with units Jy), which are obtained for each blob by summing their flooded pixel intensities and dividing by the beam volume ( $\Omega_b$ ).

`BLOBCAT` attempts to perform its internal calculations, as described in the following sections, using the fitted peak quantities  $S_p^{\text{FIT}}$  and  $A^{\text{FIT}}$ . However, if  $S_p^{\text{FIT}} < S_p^{\text{OBS}}$ , as may occur for heavily pixellated images (namely for small values of  $N_\alpha$  and  $N_\delta$  as defined in Appendix A), then for consistency `BLOBCAT` sets  $S_p^{\text{FIT}} = S_p^{\text{OBS}}$  (and thus  $A^{\text{FIT}} = S_p^{\text{OBS}}/\sigma$ ) to ensure that blobs with  $S_p^{\text{FIT}} < T_d$  yet  $S_p^{\text{OBS}} > T_d$  are not unfairly rejected from the output catalogue. For notational simplicity in subsequent discussion, we will use the superscript OBS to refer to both unfitted and fitted peak quantities; we will not distinguish between OBS and FIT quantities unless required for clarity.

We now turn to the key morphological assumption used to infer physical properties of these isolated blobs from their raw observed measurements.

## 2.3 Blob morphology assumption

In aperture synthesis imaging, individual resolution elements are described by the morphology of the dirty beam (the Fourier transform of the sampling distribution). Provided that the central core of the dirty beam can be suitably approximated by an elliptical Gaussian, the individual resolution elements in the resulting images can be described by 2D elliptical Gaussians. In other words, point sources will appear as Gaussians in an image.

In `BLOBCAT` we assume that each isolated blob is described by a 2D elliptical Gaussian characterized by a peak S/N,  $A$  and representative major and minor FWHMs  $\psi_r$  and  $\psi_s$ , respectively (representative because these FWHMs are never individually measured, as we discuss shortly). In Sections 3.3 and 4.2, we discuss situations where this assumption of Gaussian blob morphology is poor. The general equation for a 2D elliptical Gaussian, located at the origin of an arbitrary coordinate frame ( $r, s$ ) that is aligned with the major/minor axes, is given by

$$f(r, s) = A \exp \left[ -4 \ln(2) \left( \frac{r^2}{\psi_r^2} + \frac{s^2}{\psi_s^2} \right) \right]. \quad (7)$$

This equation is valid for Gaussian blobs in noise-free images of either total intensity or linear polarization. The volume of this 2D Gaussian is

$$\Omega_G = \frac{\pi A}{4 \ln 2} \psi_r \psi_s. \quad (8)$$

This general set-up, including detection thresholds as defined in Section 2.2, is shown in Fig. 2.

<sup>5</sup> <http://www.atnf.csiro.au/people/mcalabre/WCS/wcslib/>

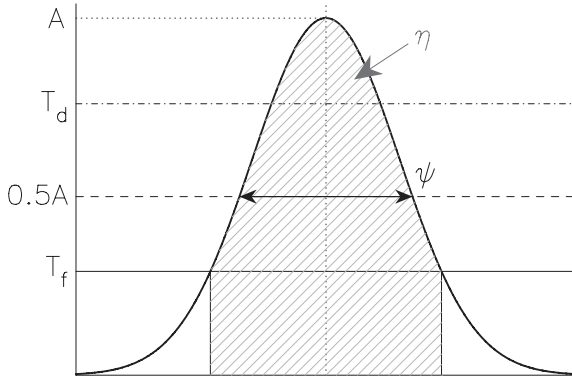


**Figure 2.** Flood fill algorithm applied to a noise-free 2D elliptical Gaussian blob with peak S/N  $A$ . The detection threshold is  $T_d$ . The blob is flooded from the peak down to the detection threshold  $T_f$ . Flood fill can only measure a fraction of the blob's total volume,  $\eta$  (equation 16), as indicated by the shading. The width of the blob at  $A/2$  (the FWHM) is  $\psi$ .

## 2.4 Blob bias corrections

BLOCAT applies two important corrections to each isolated Gaussian blob in order to prevent systematic biases from affecting its peak and integrated SB measurements. These corrections account for the following.

- (i) The positive peak SB bias exhibited by  $S_p^{\text{OBS}}$  for resolved blobs.
- (ii) The negative integrated SB bias exhibited by  $S_{\text{int}}^{\text{OBS}}$  caused by the limited blob volume accessible to flooding before the cut-off threshold  $T_f$  is reached.

### 2.4.1 Peak surface brightness bias

An illustration outlining the need for the first correction is presented in Fig. 3. To understand this bias and how to correct for it, we first examine the following experiment. Consider for simplicity that blobs are represented by tophat functions rather than 2D elliptical Gaussians, that images are produced with 1 pixel per resolution

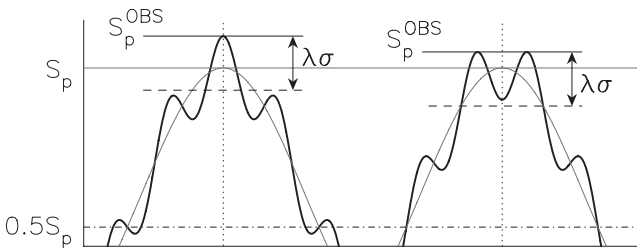


**Figure 3.** Idealized representation of the positive bias encountered when measuring the peak SB of a resolved Gaussian blob embedded in noise. Shown are two resolved Gaussian blobs, each with (true) peak SB  $S_p$  and seven resolution elements per FWHM. For visual and conceptual simplicity, noise is represented by a sine wave and it is assumed that a large number of pixels populate each resolution element (such that pixellation effects may be ignored, i.e.  $S_p^{\text{FIT}} = S_p^{\text{OBS}}$ ). Two equally likely noise superpositions are shown. The left blob encounters a positive noise contribution to its peak SB, while the right blob encounters a negative noise contribution (trough). In both cases the observed peak SB overestimates the true peak SB, leading to a systematic positive bias for resolved sources. BLOCAT corrects for this bias with equation (14), as parameterized by the area sliced at  $\lambda\sigma$  below the observed peak. If  $\lambda$  is too small, the bias correction itself may become biased due to volatility in the small area sliced, as illustrated.

element and that noise is Gaussian in character. Noise is always resolved on the same spatial scale as unresolved sources. Therefore, the peak SB of an unresolved blob, here observed as the magnitude of a single pixel, will be affected by a single noise sample which may be positive or negative. For an ensemble of such unresolved blobs, each with identical true peak SB but different noise sample, the average observed peak SB will be an unbiased tracer of the true peak SB. Now consider a resolved tophat blob, over which  $M$  independent noise samples will be present. The observed peak SB of this resolved blob will depend on the maximum of  $M$  independent noise samples, rather than  $M = 1$  for an unresolved blob. Thus, the more resolved the blob becomes, the larger  $M$  becomes and the less likely it is that a negative noise sample will be selected as the observed peak SB. The average observed peak SB for an ensemble of identically resolved blobs will therefore be positively biased from its true value. Before returning to 2D elliptical Gaussians, we will describe how to correct for this positive bias in the context of order statistics using the simpler tophat blob morphology.

For a sample of  $M$  independent and identically distributed variates  $X_1, X_2, \dots, X_M$  ordered such that  $X_{(1)} < X_{(2)} < \dots < X_{(M)}$  (using notation  $X_j$  for unordered variates and  $X_{(j)}$  for ordered variates), then  $X_{(k)}$  is known as the  $k$ th order statistic and  $X_{(M)} = \max(X_j)$ . If  $X$  has density function  $f(X)$  and distribution function  $F(X)$ , then David & Nagaraja (2003) give the density function for  $X_{(k)}$  as

$$f(X_{(k)}) = \frac{M!}{(k-1)!(M-k)!} f(X) \times [F(X)]^{k-1} [1-F(X)]^{M-k}. \quad (9)$$

The density function for the maximum of  $M$  independent Gaussian variates with variance  $\sigma^2$  is obtained from equation (9) by setting  $k = M$ , giving

$$f(X_{(M)}) = \frac{M}{\sigma\sqrt{2\pi}} \exp\left(-\frac{X^2}{2\sigma^2}\right) \left\{ \frac{1}{2} \left[ 1 + \operatorname{erf}\left(\frac{X}{\sigma\sqrt{2}}\right) \right] \right\}^{M-1}, \quad (10)$$

where erf is the error function defined by

$$\operatorname{erf}(z) = \frac{2}{\sqrt{\pi}} \int_0^z e^{-t^2} dt. \quad (11)$$

The expectation value for equation (10) is given by

$$E[f(X_{(M)})] = \int_{-\infty}^{\infty} f(X_{(M)}) dX, \quad (12)$$

which is plotted for a range of  $M$  samples in Fig. 4. Equation (12) represents the average positive bias existing between measurements of observed peak SB and true peak SB for a tophat blob. Given measurement of  $M$ , namely the number of independent resolution

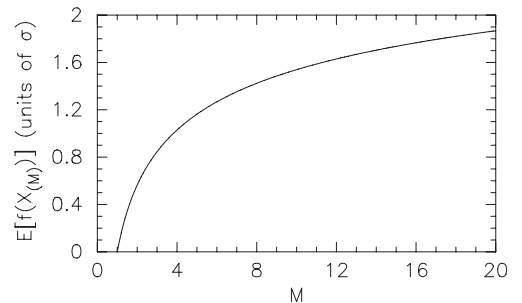


**Figure 4.** Expectation value in noise units of  $\sigma$  for the largest of  $M$  independent Gaussian variates (equation 12). The expectation value is 0 for  $M = 1$ . A polynomial fit to the curve is given by equation (14).

elements present over the extent of the blob, an estimate for the bias can be obtained. The bias is most pronounced for low-S/N resolved blobs; for a tophat blob of extent  $\sim 4$  resolution elements, the bias for a  $5\sigma$  blob is  $\sim 1.0\sigma/5\sigma = 20$  per cent (see Fig. 4).

We now return to the scenario whereby blobs are assumed to represent 2D elliptical Gaussians. Instead of obtaining  $M$  from the full spatial extent of a tophat blob,  $M$  needs to be estimated from the observable properties of a 2D Gaussian embedded in noise. In `BLOBCAT` we estimate  $M$  by approximating that the relevant number of independent resolution elements contributing to the positive bias can be extracted from the cross-sectional area contained within a slice of constant S/N at a few  $\sigma$  below the peak, as parametrized by  $\lambda$  in Fig. 3. `BLOBCAT` measures the cross-sectional area for each blob at  $S/N = (A^{\text{OBS}} - \lambda)$ , which we denote  $H_\lambda$ , by flooding from the peak to this threshold and simply counting the number of pixels present.  $M$  is then estimated using (cf. equation 3)

$$M = \frac{\bar{d}}{\Omega_b} H_\lambda. \quad (13)$$

To determine the positive bias between  $S_p^{\text{OBS}}$  and  $S_p$  for resolved blobs, `BLOBCAT` uses the following fifth-order polynomial fit to the curve in Fig. 4 to form a simple lookup table (rather than solving for equation 12),

$$M = 1 + \sum_{i=1}^5 a_i \beta^i, \quad (14)$$

where

$$\beta = E[f(X_{(M)})] \approx \frac{S_p^{\text{OBS}}}{S_p} \left( = \frac{A^{\text{OBS}}}{A} \right), \quad (15)$$

and where  $a_1 = 0.89$ ,  $a_2 = 0.27$ ,  $a_3 = 3.75$ ,  $a_4 = -3.67$  and  $a_5 = 1.61$ .

To illustrate the constraints on selecting  $\lambda$ , imagine trying to correct the raw observed peak SB for a resolved Gaussian blob, detected with peak  $S/N = 50$ , by arbitrarily defining that the relevant spatial extent be measured at  $\lambda = 20$ . Choosing  $M$  in this way will overestimate the peak's positive bias, because not even a  $10\sigma$  noise spike located at the  $S/N = 30$  contour of the blob could be mistaken for the true peak. Alternatively, choosing too small a value of  $\lambda$  will not only underestimate the peak bias in the opposite manner to above, but also render  $M$  vulnerable to additional negative bias due to  $H_\lambda$  being fooled (limited in spatial extent) by noise troughs near the blob's peak.

We performed simulations to empirically determine the most suitable range of values for  $\lambda$ . We found that choosing  $\lambda = 3.5$  best corrected for the positive bias exhibited by  $S_p^{\text{OBS}}$  for resolved blobs in images of either total intensity or linear polarization ( $L$  or  $L_{\text{RM}}$ ). We discuss the simulations used to determine this optimum  $\lambda$ , as well as the general performance of the peak SB bias correction from equation (14), in Section 3.

#### 2.4.2 Integrated surface brightness bias

To prevent the flood fill algorithm from cascading into noise features adjacent to real blobs, flooding is terminated at the cut-off threshold,  $T_f$ . The integrated SB measured for each blob,  $S_{\text{int}}^{\text{OBS}}$ , therefore underestimates the true integrated SB,  $S_{\text{int}}$ , because only a limited fraction of the total volume for each blob is ever directly accessed. We denote this fraction  $\eta$ , as indicated in Fig. 2.

By integrating the volume flooded between  $A$  (true peak S/N) and  $T_f$  for a 2D elliptical Gaussian blob, and dividing this result by

the total volume of the blob (equation 8), the fraction of flooded volume  $\eta$  is found to be

$$\eta = \left( \text{erf} \sqrt{-\ln \frac{T_f}{A}} \right)^2. \quad (16)$$

`BLOBCAT` corrects the observed integrated SB for each detected blob (regardless of blob dimension) by simply dividing by  $\eta$ , namely

$$S_{\text{int}} = \frac{S_{\text{int}}^{\text{OBS}}}{\eta}. \quad (17)$$

It is important to note that  $A$  in equation (16) is the true peak S/N. For resolved blobs, the peak bias correction from equation (14) needs to be applied first, so as to debias the observed peak S/N,  $A^{\text{OBS}}$ , and return an estimate for the unbiased peak S/N,  $A$ . The effect of using uncorrected peak S/N values for resolved sources in equation (16) is demonstrated in Section 3.

The choice of  $T_f$  affects the maximum volume that can be flooded within a faint blob. To recommend a minimum value, we performed simulations of integrated SB recovery for 2D elliptical Gaussian blobs embedded within images of total intensity and linear polarization; the details of these simulations are discussed in Section 3. We incrementally reduced  $T_f$  in these simulations, seeking a balance between the measurement of as much volume as possible within faint blobs, and the need to avoid bias from potential overflowing of neighbouring noise features.

In total intensity images for blobs as faint as  $A = 5$ , we found that a cut-off threshold of  $T_f = 2.6$  was required in order to robustly flood as many true blob pixels as possible whilst avoiding overflowing of adjacent non-blob (noise) pixels. In linear polarization images ( $L$  or  $L_{\text{RM}}$ ), non-Gaussian noise statistics typically limit detection thresholds to  $T_d \gtrsim 6$  (Vaillancourt 2006; Hales et al. 2012). These images thus require higher flooding thresholds than those for total intensity; we note that a comparison between the average cross-sectional profile of a Gaussian blob embedded in images exhibiting Gaussian,  $L$ , and  $L_{\text{RM}}$  statistics is presented by Hales et al. (2012). In images of  $L_{\text{RM}}$  for blobs as faint as  $A = 6$ , we found that a cut-off threshold of  $T_f = 4.0$  was suitable. We note that this value of  $T_f$  is dependent on the observational set-up used to produce  $L_{\text{RM}}$ . To determine an equivalent value of  $T_f$  for any  $L$  or  $L_{\text{RM}}$  image, a cut-off with equal statistical significance to our suggested  $T_f = 4.0$  value should be calculated (e.g. see Hales et al. 2012).

For a detection threshold of  $T_d = 5$  in an image of total intensity, equation (16) with  $T_f = 2.6$  implies that the maximum correction factor for any blob is  $1/\eta \lesssim 1.8$ . In linear polarization, for a detection threshold of  $T_d \sim 6$  and  $T_f = 4.0$ , the maximum correction factor is  $1/\eta \lesssim 2.5$ .

## 2.5 Program inputs

If accurate error estimates are not immediately required, `BLOBCAT` does not require many inputs to run. Preliminary analysis can be performed on a single input SB image by specifying three parameters: a background rms noise value (simply so that S/N values can be computed at any spatial location within the image), a blob detection S/N threshold ( $T_d$ ) and a cut-off S/N threshold for flooding ( $T_f$ ). However, to make full use of the output catalogue, particularly errors, additional input parameters are required. For completeness, we list all `BLOBCAT` input arguments in Appendix B.

## 2.6 Output catalogue

BLOBCAT produces an output catalogue containing 41 entries for each detected blob. In this section we list and define these entries, which include final measurements of peak and integrated SB, corrected for bandwidth smearing and clean bias, errors and the ‘visibility’ area for each blob. The catalogue entries, some of which require various BLOBCAT input arguments to be specified (see Appendix B), are as follows.

*Column 1: ID*

Blob identification number, ordered by decreasing observed peak S/N (see column 26).

*Column 2: npix*

Number of flooded pixels comprising blob.

*Columns 3 and 4: x\_p, y\_p*

RA and Dec. of peak pixel in pixel coordinates.

*Columns 5 and 6: RA\_p, Dec\_p*

RA and Dec. of peak pixel in degrees.

*Column 7: RA\_p\_err*

Total position error in RA of peak pixel, which we define as

$$\sigma_\alpha = \sqrt{\sigma_{\alpha,\text{cal}}^2 + \sigma_{\alpha,\text{frame}}^2 + \sigma_{\alpha,\text{blob}}^2} \quad (18)$$

The first term,  $\sigma_{\alpha,\text{cal}}^2$ , represents the positional uncertainty of the phase calibrator, for example with reference to the International Celestial Reference Frame, that was used to produce the SB image. The second term,  $\sigma_{\alpha,\text{frame}}^2$ , represents the positional uncertainty of the image frame about the (assumed) position of the phase calibrator. Given that image positional errors correspond to Fourier-plane phase errors,  $\sigma_{\alpha,\text{frame}}^2$  may be estimated by measuring  $\sigma_{\text{SEM}}$ , the standard error of the mean (SEM) of the variation in the phase corrections resulting from phase self-calibration<sup>6</sup> (Cornwell & Fomalont 1999). By estimating the fraction of a resolution element by which positions may be in error as  $\sigma_{\text{SEM}}/180^\circ$ , BLOBCAT estimates the frame error as

$$\sigma_{\alpha,\text{frame}} \approx \frac{1}{\sqrt{2}} \frac{\sigma_{\text{SEM}}}{180^\circ} \Theta_\alpha, \quad (19)$$

where the factor of  $\sqrt{2}$  projects the 2D SEM along one of the two orthogonal axes and  $\Theta_\alpha$  is the projected resolution along the RA-axis.  $\Theta_\alpha$  is given by

$$\Theta_\alpha = \frac{\Theta_{\text{maj}} \Theta_{\text{min}}}{\sqrt{(\Theta_{\text{maj}} \cos \chi)^2 + (\Theta_{\text{min}} \sin \chi)^2}}, \quad (20)$$

where  $\chi$  is the position angle of the major axis east of north. The third term,  $\sigma_{\alpha,\text{blob}}^2$ , encapsulates positional error due to the significance of the blob detection, which we define for reasons described later in Sections 3.1.3 and 3.2.3 as

$$\sigma_{\alpha,\text{blob}} \approx \frac{1}{1.4 A} \Theta_\alpha. \quad (21)$$

*Column 8: Dec\_p\_err*

Total position error in Dec. of peak pixel, which we define in a similar manner to equation (18) as

$$\sigma_\delta = \sqrt{\sigma_{\delta,\text{cal}}^2 + \sigma_{\delta,\text{frame}}^2 + \sigma_{\delta,\text{blob}}^2}, \quad (22)$$

<sup>6</sup> Note that regardless of whether or not self-calibration phase corrections are applied to the visibility (Fourier) data prior to final imaging (i.e. it is possible to calculate the required phase corrections without applying them), the systematic positional offset between the image frame and the phase calibrator can be characterized by the SEM of the phase corrections (e.g. Hales et al. 2009).

where

$$\sigma_{\delta,\text{frame}} \approx \frac{1}{\sqrt{2}} \frac{\sigma_{\text{SEM}}}{180^\circ} \Theta_\delta, \quad (23)$$

$$\sigma_{\delta,\text{blob}} \approx \frac{1}{1.4 A} \Theta_\delta, \quad (24)$$

and where the projected resolution along the Dec.-axis is given by

$$\Theta_\delta = \frac{\Theta_{\text{maj}} \Theta_{\text{min}}}{\sqrt{(\Theta_{\text{maj}} \sin \chi)^2 + (\Theta_{\text{min}} \cos \chi)^2}}. \quad (25)$$

*Columns 9 and 10: x\_c, y\_c*

RA and Dec. of area (unweighted) centroid in pixel coordinates,

$$(x_c, y_c) = \frac{\sum_{i=1}^{\text{npix}} \mathbf{x}_i}{\text{npix}}, \quad (26)$$

where  $\mathbf{x}_i = (x_i, y_i) \in \text{blob}$ .

*Columns 11 and 12: RA\_c, Dec\_c*

RA and Dec. of unweighted centroid in degrees.

*Column 13: cFlag*

Centroid flag. If  $(x_c, y_c)$  is located within a flooded pixel, then cFlag = 1; otherwise cFlag = 0.

*Columns 14 and 15: x\_wc, y\_wc*

RA and Dec. of S/N-weighted centroid in pixel coordinates,

$$(x_{\text{wc}}, y_{\text{wc}}) = \frac{\sum_{i=1}^{\text{npix}} \mathbf{x}_i A^{\text{OBS}}(\mathbf{x}_i)}{\sum_{i=1}^{\text{npix}} A^{\text{OBS}}(\mathbf{x}_i)}. \quad (27)$$

*Columns 16 and 17: RA\_wc, Dec\_wc*

RA and Dec. of S/N-weighted centroid in degrees.

*Column 18: wcFlag*

Weighted centroid flag. If  $(x_{\text{wc}}, y_{\text{wc}})$  is located within a flooded pixel, then wcFlag = 1; otherwise wcFlag = 0. If wcFlag = 1, then RA\_wc and Dec\_wc from columns 16 and 17 above are the formal positions of the blob. If wcFlag = 0, the blob is likely to be significantly non-Gaussian; the weighted-centroid position may not be suitable for formal cataloguing purposes. Manual inspection, or formal cataloguing using the raw peak pixel or area centroid positions, may be required.

*Columns 19–22: x\_min, x\_max, y\_min, y\_max*

The minimum and maximum pixel coordinates in RA ( $x$ ) and Dec. ( $y$ ) within blob.

*Column 23: rms*

rms noise,  $\sigma$ , at the position of peak pixel.

*Column 24: BWScorr*

Bandwidth smearing correction,  $1/\varpi$  (from equation 6).

*Column 25: M*

Number of independent resolution elements from equation (13).  $M$  is used in equation (14) to correct for the positive peak bias exhibited by resolved blobs. To prevent this bias correction from being applied to noise-affected unresolved blobs (i.e. where the number of pixels flooded is artificially boosted due to a connected noise feature), BLOBCAT only applies the correction to those blobs with  $M \geq 1.1$ ; the suitability of this value was determined empirically.

*Column 26: SNR\_OBS*

Observed (raw) S/N,  $A^{\text{OBS}} = S_p^{\text{OBS}}/\sigma$ .

*Column 27: SNR\_FIT*

Fitted S/N,  $A^{\text{FIT}} = S_p^{\text{FIT}}/\sigma$ .

*Column 28: SNR*

S/N,  $A$ , corrected for peak bias (equation 14).

*Column 29: S\_p\_OBS*

Observed (raw) peak SB,  $S_p^{\text{OBS}}$ .



**Column 30: S\_p\_FIT**

Fitted peak SB,  $S_p^{\text{FIT}}$ , obtained using a 2D parabolic fit to a  $3 \times 3$  pixel array about the raw peak pixel  $(x_p, y_p)$ . If  $S_p^{\text{FIT}} < S_p^{\text{OBS}}$ , then `BLOBCAT` sets  $S_p^{\text{FIT}} = S_p^{\text{OBS}}$  so as to use the more accurate measurement (see Appendix A and Section 2.2).

**Column 31: S\_p**

Peak SB,  $S_p$ , corrected for peak bias (equation 14).

**Column 32: S\_p\_CB**

Peak SB corrected for peak bias and clean bias,  $S_p^{\text{CB}}$ . Clean bias is a deconvolution effect that redistributes SB from real blobs to noise peaks, systematically reducing the observed SB of blobs independent of their S/N (Condon et al. 1998). The effect is more pronounced for observations with poor Fourier-plane coverage. Given the degree of clean bias present in the SB image,  $\Delta S^{\text{CB}}$  ( $\geq 0$  Jy beam $^{-1}$ ), `BLOBCAT` makes the following correction:

$$S_p^{\text{CB}} = S_p + \Delta S^{\text{CB}}. \quad (28)$$

**Column 33: S\_p\_CBBWS**

Peak SB corrected for peak bias, clean bias and bandwidth smearing,  $S_p^{\text{CB,BWS}}$ . Using the input value of  $\varpi$  (equation 6), `BLOBCAT` corrects for bandwidth smearing with

$$S_p^{\text{CB,BWS}} = \frac{S_p^{\text{CB}}}{\varpi}. \quad (29)$$

This is the final reported value of the blob's peak SB, to be used for post-processing.

**Column 34: S\_p\_CBBWS\_err**

Error in corrected peak SB, which we define as

$$\sigma_{S_p^{\text{CB,BWS}}} = \left[ \left( \Delta S^{\text{ABS}} S_p^{\text{CB,BWS}} \right)^2 + \left( \Delta S^{\text{PIX}} S_p^{\text{CB,BWS}} \right)^2 + \left( \frac{\sigma}{\varpi} \right)^2 \right]^{1/2}, \quad (30)$$

where  $\Delta S^{\text{ABS}}$  is the absolute calibration error of the SB image and  $\Delta S^{\text{PIX}}$  is the pixellation uncertainty (see Appendices A and B). The suitability of this error in linear polarization is discussed in Section 3.2.

**Column 35: S\_int\_OBS**

Observed (raw) integrated SB,  $S_{\text{int}}^{\text{OBS}}$ .

**Column 36: S\_int\_OBSCB**

Observed integrated SB corrected for clean bias, given by

$$S_{\text{int}}^{\text{OBS,CB}} = S_{\text{int}}^{\text{OBS}} + \frac{\text{npix} \Delta S^{\text{CB}}}{\Omega_b}. \quad (31)$$

This value may be useful for non-Gaussian blobs (see Section 3.3).

**Column 37: S\_int**

Integrated SB,  $S_{\text{int}}$ , calculated by the application of blob volume correction (equation 17) to  $S_{\text{int}}^{\text{OBS,CB}}$ .

**Column 38: S\_int\_CB**

Integrated SB corrected for clean bias,  $S_{\text{int}}^{\text{CB}}$ , calculated by the application of blob volume correction (equation 17) to  $S_{\text{int}}^{\text{OBS,CB}}$ . This is the final reported value of the blob's integrated SB, to be used for post-processing (though see comments in Section 3.3).

**Column 39: S\_int\_CB\_err**

Error in corrected integrated SB, which we define in a similar manner to `S_p_CBBWS_err` (see also Section 3.1) as

$$\sigma_{S_{\text{int}}^{\text{CB}}} = \sqrt{\left( \Delta S^{\text{ABS}} S_{\text{int}}^{\text{CB}} \right)^2 + \sigma^2}. \quad (32)$$

The suitability of this error in linear polarization is discussed in Section 3.2.

**Column 40: R\_EST**

Size estimate of detected blob,  $R^{\text{EST}}$ , in units of the sky area covered by an unresolved Gaussian blob with the same peak SB, taking into account local bandwidth smearing. To derive this estimate we first focus on an unresolved Gaussian blob with FWHM  $\Theta$ , as defined by the image resolution and peak SB  $S_p$ , as measured from the detected blob. For this unresolved blob, the relationship between its full width at a fraction  $T_f/A$  of its peak SB, which we denote  $\varphi$ , and its FWHM is given by

$$\varphi = \Theta \sqrt{\log_2 \frac{A}{T_f}}. \quad (33)$$

To calculate  $R^{\text{EST}}$  we take the ratio between the measured area of the detected blob,  $H_{\text{blob}}$ , and the area of an ellipse with axes defined by equation (33). When the broadening effect of bandwidth smearing is included into this ratio, we get

$$R^{\text{EST}} = H_{\text{blob}} \left( \frac{\pi \Theta_{\text{maj}} \Theta_{\text{min}}}{4 \varpi} \log_2 \frac{A}{T_f} \right)^{-1}. \quad (34)$$

The parameter  $R^{\text{EST}}$  is not intended to be used for quantitative analysis. In Section 4, we discuss how  $R^{\text{EST}}$  may be used to flag blobs that exhibit potentially complex (non-Gaussian) morphologies for follow-up.

**Column 41: VisArea** `BLOBCAT` can optionally calculate the fraction of visible sky area, namely the fraction of non-blank pixels assuming the use of an equal-area projection, over which a blob detected at position  $(r, s)$  could have been detected within the SB image. This is known as the blob's visibility area. This area may be used, for example, to calculate a completeness correction when compiling source counts (e.g. Hales et al., in preparation). To calculate the visibility area, `BLOBCAT` takes into account spatial variations in both image sensitivity and bandwidth smearing. For non-blank pixels  $(x, y)$ , the fraction of suitable sky area for detecting a blob with equal peak SB to that of a blob located at  $(r, s)$ , where  $r \in x, s \in y$ , is obtained by counting the number of pixels that satisfy

$$\frac{T_d \sigma(x, y)}{\varpi(x, y)} \leq \frac{S_p(r, s)}{\varpi(r, s)}. \quad (35)$$

## 2.7 Optional outputs

To aid visual inspection and post-processing of blobs, `BLOBCAT` can optionally produce two additional forms of output. The first is a modified SB FITS image in which all flooded pixels have been highlighted (reset to a large value; this value may be user-specified, see Appendix B). The second is an image overlay in `ds9` (Joye & Mandel 2003) or `Karma` (Gooch 1996) formats, for use with their respective `ds9` or `kvis` FITS viewers. The overlays present the identification number and boundaries in RA and Dec. for each blob. To illustrate these two optional forms of output, an example output FITS image superposed with a `kvis` overlay is presented in Fig. 5. `BLOBCAT` may be easily modified to produce overlays in other suitable formats, for example through the use of the `pywcs` wrapper to `WCSSLIB`.

## 3 PERFORMANCE

We have carried out Monte Carlo simulations to investigate the performance of `BLOBCAT` in total intensity and linear polarization, as described in the following sections.

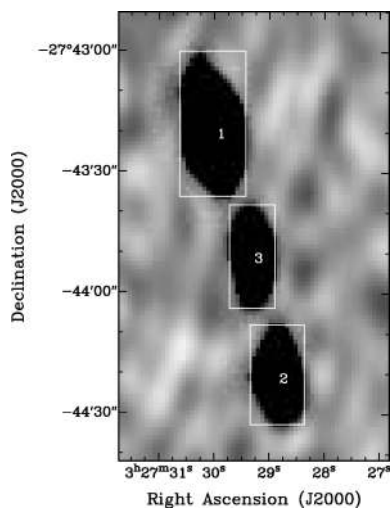


**Figure 5.** Output FITS image and *kvis* overlay as produced by BLOCAT, illustrating how three blobs in the image are highlighted and identified (sample data from Norris et al. 2006).

### 3.1 Total intensity

#### 3.1.1 Simulation set-up

We tested BLOCAT in total intensity by injecting Gaussian sources with peak S/N values between  $5\sigma$  and  $100\sigma$  into images of Gaussian noise, inspecting the accuracy of the recovered SB and positional measurements. To compare BLOCAT's flood fill approach with that of standard Gaussian fitting, we also carried out these simulations using IMFIT, a widely used Gaussian source fitter from the MIRIAD package (Sault et al. 1995). Gaussian fitting routines such as IMFIT have been used by many surveys such as NVSS (Condon et al. 1998), Phoenix (Hopkins et al. 2003) and SUMMS (Mauch et al. 2003).

Two classes of source were tested, with the aim of demonstrating the virtues and limitations of BLOCAT's modified flood fill approach. The first were unresolved (point) sources, selected to demonstrate that flood fill algorithms need not be limited to the parameter space occupied by complex non-Gaussian sources. The second were highly (and somewhat pathologically) resolved Gaussian sources with FWHMs five times larger than the image resolution, probing parameter space where parametrized Gaussian fitting methods are optimal. We did not quantitatively address performance relating to non-Gaussian sources because of the lack of an obvious standardized test source; qualitative discussion of non-Gaussian blobs is presented in Section 3.3.

We generated 125 independent samples per S/N bin using noise images produced as follows. To realistically characterize the noise environment present in images of total intensity, we obtained Stokes *V* data from an individual pointing of the mosaicked 1.4-GHz aperture synthesis observations of Norris et al. (2006). We imaged these Stokes *V* data using 1 arcsec pixels and convolved to a final circular resolution with (FWHM)  $\Theta = 14$  arcsec. We found this image to be free of sources and artefacts. Using SExtractor (see Section 2.1.2), we modified this Stokes *V* image for use as a master noise image by enforcing zero mean and unit variance throughout subregions of size 150 independent resolution elements. The noise image for each sample was then produced by extracting a randomly positioned thumbnail image from the master noise image, from a pool of over 150 000 choices.

For each sample we measured the injected source's peak SB, integrated SB and position using both BLOCAT and IMFIT. We executed IMFIT using unconstrained Gaussian fit parameters, imitating a blind survey. For input point sources, we also executed IMFIT using a constrained fit, fixing the source size to the image resolution. We then compared the output values for these different methods with their true input values. To prevent source misidentification, we checked that each recovered source extended over its true input location. We describe the results of these Monte Carlo simulations for SB measurements in Section 3.1.2 and for positions in Section 3.1.3.

#### 3.1.2 Results and discussion: surface brightness measurements

We performed our total intensity Monte Carlo simulations for a range of flooding thresholds ( $T_f$ ) and peak bias correction factors ( $\lambda$ ), setting the detection threshold ( $T_d$ ) as small as possible so as to limit the induction of sampling bias in the lowest S/N bins. For reasons outlined in Sections 2.4.1 and 2.4.2, we found that optimal SB recovery was obtained using  $T_f = 2.6$  and  $\lambda = 3.5$ .

In Fig. 6 we present the SB results of our simulations, where we have executed BLOCAT with the optimal  $T_f$  and  $\lambda$  values from above, we have executed IMFIT with unconstrained Gaussian fit parameters, and where we have used median statistics (Tukey 1977) to robustly prevent noise outliers from biasing intrinsic source extractor properties. The results obtained from executing IMFIT with constrained point source fits, using the same simulation data as for the unconstrained fits, are presented in Fig. 7. To put BLOCAT's performance

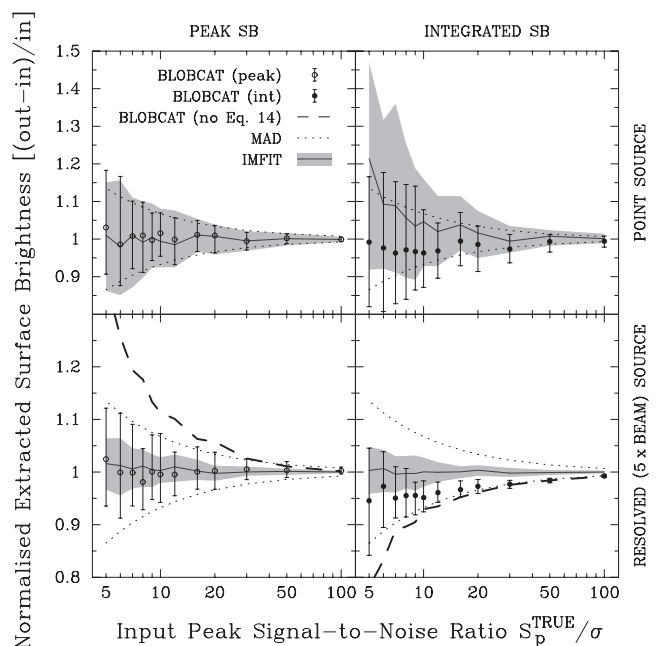


**Figure 6.** Performance of BLOCAT (points) and IMFIT (shading) in total intensity for input unresolved (top row) and resolved (FWHM =  $5 \times$  image resolution; bottom row) Gaussian sources. Measurements of peak (left-hand column) and integrated (right-hand column) SB over a range of input peak S/N values are summarized by their median (points/curves) and first and third quartiles (whiskers/shading). Dashed curves trace median measurements resulting from exclusion of the peak bias correction for resolved sources (equation 14). Fit parameters for IMFIT are unconstrained. For reference, expected random errors are indicated by the median absolute deviation (MAD  $\approx 0.6745\sigma$ ; dotted curves). Note that the y-axis range differs between rows.

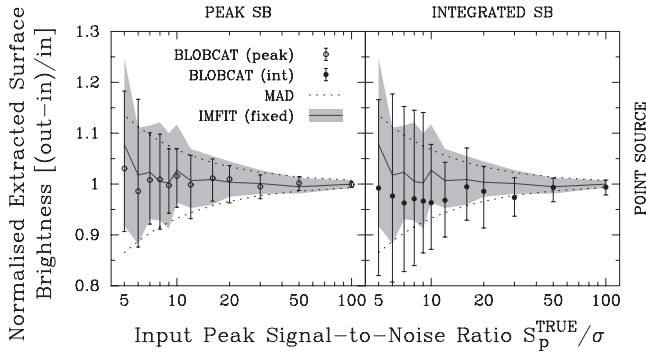


**Figure 7.** Reproduction of the top row of Fig. 6, but here displaying IMFIT results for point source fits with angular dimensions fixed to the image resolution.

in perspective, we first discuss the results from IMFIT, starting with the unconstrained fits from Fig. 6.

The strength of IMFIT is its ability to perform least-squares fitting in order to separate smooth underlying 2D elliptical Gaussians from superposed noise fluctuations. A key requirement of this process is that there are sufficient degrees of freedom (DOFs) to fit the position, peak SB, major and minor axes and position angle parameters. Given that the number of DOFs is related to the number of independent resolution elements within the fitting region, it is to be expected that IMFIT will struggle to constrain multiple fit parameters for point-like input sources. This is reflected in the IMFIT results from Fig. 6, where the systematic bias in integrated SB measurements for point sources (top-right panel;  $\gtrsim 15$  per cent at  $5\sigma$ ) demonstrates IMFIT’s inability to simultaneously constrain peak SB and angular dimension parameters. For these point sources, which by definition have the dimensions of a single resolution element and therefore contain essentially one piece of information, namely their brightness, least-squares fitting is easily coerced into including adjacent noise peaks into the fit. However, for resolved sources, which by definition extend over multiple independent resolution elements, least-squares fitting becomes less likely to misinterpret noise features as true signal and so becomes more accurate.

The systematic positive bias exhibited by IMFIT in its measurements of integrated SB for point sources leads to two systematic effects. First, given that the integrated to peak SB ratio is typically used to select which measure best characterizes the flux density of a source (e.g. Huynh et al. 2005), the flux densities of faint sources will be systematically overestimated. Secondly, this ratio is often used to estimate deconvolved angular source sizes (e.g. Huynh et al. 2005), which too will become positively biased for faint sources. We comment on this ratio further in Section 4.1.

We now turn to IMFIT’s performance from Fig. 7. When there is prior knowledge that a source is unresolved, IMFIT can be constrained to fit a point source, fixing its fitted dimensions to those of the image resolution. Comparing the results from Fig. 6 with those of Fig. 7, we find that the point source assumption reduces IMFIT’s integrated SB bias, but does not completely eliminate it. Left behind is a marginal positive bias at low input S/N, caused by IMFIT’s residual-minimization strategy to pull fitted sources towards noise peaks that are directly adjacent to true source peaks. We comment further on measured positions in Section 3.1.3.

Returning to the BLOBCAT results from Fig. 6, we find that the recovered peak and integrated SB measurements for point sources are systematically unbiased. This performance enhancement over IMFIT is due to the reduced influence that nearby noise features can

exert over BLOBCAT’s integrated SB measurements. Only directly connected noise features can affect flood fill, when the algorithm spills into adjacent noise peaks and is eventually limited by  $T_f$ , whereas strong noise peaks separated by a noise trough from the true source may be least-squares minimized by IMFIT as statistical fluctuations superposed on a resolved source.

For the resolved source investigated, IMFIT clearly outperforms BLOBCAT in avoiding integrated SB systematics. However, BLOBCAT’s systematic underestimate is no worse than  $\sim 5$  per cent, even for sources with peak  $S/N = 5$ . As indicated in Fig. 6, this underestimate would be more severe if the peak bias correction from equation (14) were neglected; failure to debias the peak SB causes equation (17) to underestimate the integrated SB. We attribute BLOBCAT’s difficulty in collecting the full integrated SB for resolved sources to an analogous ‘negative’ version of our peak SB correction. As sources become more resolved, it becomes more likely that negative noise features may limit the spatial extent available for the flood fill algorithm to explore. This behaviour is not completely offset by positive noise features contributing to the spatial extent of sources, and so a bias is produced. Given how mild the resulting bias is, even for the pathologically resolved source tested, we do not attempt to correct for it within BLOBCAT.

To estimate the uncertainty in BLOBCAT’s measurements of peak and integrated SB, we use equations (30) and (32). These errors are indicated by dotted lines in Fig. 6; we neglect the absolute calibration error ( $\Delta S^{\text{ABS}}$ ), and set the pixellation error ( $\Delta S^{\text{PIX}}$ ) to 0.5 per cent (cf. Appendix A). We do not reduce the factor of  $\sigma$  in equation (32) by, for example, the square root of the number of independent resolution elements within the spatial extent of the source, as might be appropriate for methods that produce systematically unbiased integrated SB measurements. Instead, we define equation (32) in a similar manner to equation (30), so as to artificially account for BLOBCAT’s systematic underestimate of integrated SB for resolved sources. In this way, the error estimates produced by BLOBCAT realistically encapsulate its true performance. Note that, in practice, resolved sources will almost always be less resolved than for our simulated resolved source here. This implies that our catalogue error estimates are unlikely to underestimate true SB measurement errors.

### 3.1.3 Results and discussion: position measurements

BLOBCAT catalogues three positions for each detected blob: the raw peak pixel, an area centroid using equation (26) and an S/N-weighted centroid using equation (27). In Fig. 8 we compare the accuracy of these measurements, as well as position measurements from IMFIT, in recovering the true input positions for our simulated unresolved and resolved sources.

Fig. 8 indicates that of BLOBCAT’s three position measurements, the weighted centroid is optimal for both unresolved and resolved Gaussian sources. The superior performance of the peak pixel position for unresolved sources is an artefact of injecting sources centred on a pixel; in general, the performance of this position measure will be poorer. For resolved sources, the raw peak position is easily corrupted by the peak bias effect described earlier in Section 2.4.1. For both unresolved and resolved Gaussian sources, the area centroid exhibits limited accuracy due to its lack of pixel weighting.

For faint unresolved sources, BLOBCAT’s positions are more accurate than those of IMFIT’s unconstrained Gaussian fits; IMFIT is limited in its accuracy due to its optimization attempts to accommodate adjacent noise features through least-squares minimization.

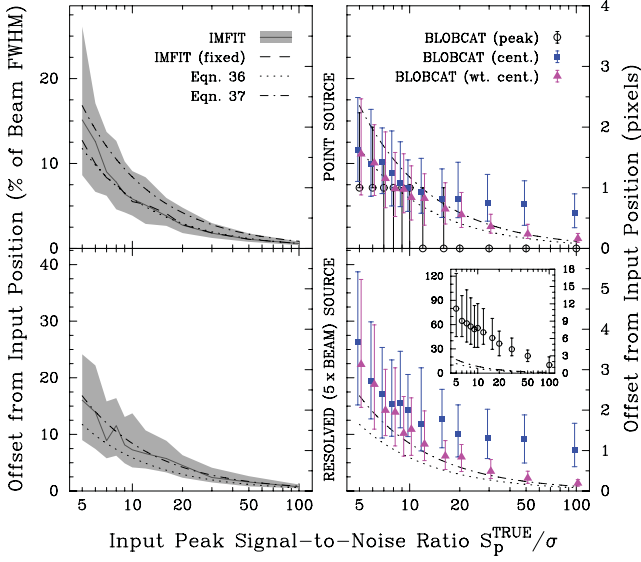


**Figure 8.** Accuracy of positions measured by *IMFIT* (shading; left column) and *BLOCAT* (points for the peak pixel, centroid and S/N-weighted centroid; right-hand column) in total intensity for input unresolved (top row) and resolved (bottom row) Gaussian sources; median statistics are displayed (similar formalism to Fig. 6). The dashed curve (top-left panel) traces median measurements for constrained *IMFIT* point source fits with angular dimensions fixed to the image resolution. For reference, the dotted and dot-dashed curves (identical in each panel) indicate expected median positional offsets using equations (36) and (37), respectively. The left y-axis for each panel denotes position offset from the true input source position in units of the circular resolution FWHM ( $\Theta = 14$  arcsec); the right y-axis denotes this offset in units of pixel width (1 arcsec). Note that the y-axis range differs between rows. For clarity, the bottom-right panel shows only centroid and S/N-weighted centroid measurements; the inset provides peak pixel measurements in a zoomed-out view of this panel.

For the pathologically resolved source simulated, *IMFIT*'s position measurements are more accurate than *BLOCAT*'s.

To estimate the uncertainty in *BLOCAT*'s weighted centroid positions, we first look to an uncertainty estimate for *IMFIT*. For plotting purposes, the median positional offset exhibited by *IMFIT* can be estimated as the median of the quadrature sum of two zero-mean signals representing RA and Dec. measurements with error  $\sigma_\alpha$  (equation 18) and  $\sigma_\delta$  (equation 22), respectively. By using a factor of  $\sqrt{8 \ln 2} \approx 2$  instead of 1.4 in equations (21) and (24) as suggested for Gaussian fitting by Condon (1997), neglecting calibration and frame errors, using  $\Theta = \Theta_\alpha = \Theta_\delta$  for a circular beam, and noting that the median offset about an input position in 2D is given by the median of a Rayleigh (1880) distribution, we evaluate the expected median positional offset for *IMFIT* as

$$\text{pos.offset}_{\text{median}}^{\text{C97}} = \sqrt{\ln 4} \frac{\Theta}{2A}. \quad (36)$$

This estimate is indicated by the dotted curve in each panel of Fig. 8.

Equation (36) suitably encapsulates the positional uncertainties exhibited by both *IMFIT* and *BLOCAT* for unresolved sources. However, for our heavily resolved source, it systematically underestimates the positional uncertainties exhibited by both the Gaussian fit and flood-fill approaches. To avoid complexity, we do not attempt to explicitly parameterize the increased positional uncertainty displayed for resolved sources. Instead, we have chosen to simply modify the positional uncertainty equations presented by Condon (1997) to use a factor of 1.4 (instead of  $\sim 2$ ), as presented in equations (21) and (24). These modified equations lead to a more appropriate estimate

for the median positional offset,

$$\text{pos.offset}_{\text{median}}^{\text{BLOCAT}} = \sqrt{\ln 4} \frac{\Theta}{1.4A}, \quad (37)$$

as indicated by the dot-dashed curve in each panel of Fig. 8. The factor of 1.4 was selected empirically to ensure that for Gaussian sources with sizes ranging from unresolved to the heavily resolved source tested, positional uncertainties may be systematically estimated to within  $\sim 5$  per cent of a beam FWHM. We note that the factor of 1.4 is also suitable for use with *IMFIT* (see the left-hand panels in Fig. 8).

## 3.2 Linear polarization

### 3.2.1 Simulation set-up

We tested *BLOCAT* in linear polarization,  $L_{\text{RM}}$ , in a similar manner to that described in Section 3.1.1 for total intensity. We tested the same two classes of source, sampling input peak S/N values between  $6\sigma_{\text{RM}}$  and  $100\sigma_{\text{RM}}$  (cf. equation 5; also Section 2.4.2). For comparison, we also tested the performance of *IMFIT* using both constrained and unconstrained Gaussian fit parameters.

We generated each of the 125 sample images per S/N bin as follows. We assumed an illustrative observational band centred on 1396 MHz with width 200 MHz, split into  $25 \times 8$  MHz channels. For each frequency channel we obtained two independent noise thumbnails from the master noise image (cf. Section 3.1.1), which we used to represent Stokes  $Q$  and  $U$  noise. A point (or resolved) source with an RM of  $-100 \text{ rad m}^{-2}$ , unresolved in Faraday space, was then suitably injected into each of the Stokes  $Q$  and  $U$  images across the band. We define the peak S/N of these injected sources as the ratio between their true input peak polarized SB and  $\sigma_{\text{RM}}$ . Using RM synthesis (Brentjens & de Bruyn 2005) and *RM CLEAN* (Heald et al. 2009), images of  $L_{\text{RM}}$  were then produced in accordance with equation (1). For each sample, we then recovered the peak and integrated SB using both *BLOCAT* and *IMFIT*. We describe the results of these Monte Carlo simulations for SB measurements in Section 3.2.2 and for positions in Section 3.2.3.

### 3.2.2 Results and discussion: surface brightness measurements

We performed our linear polarization Monte Carlo simulations using a range of  $T_d$ ,  $T_f$  and  $\lambda$  parameter values, finding that the optimal total intensity value of  $\lambda = 3.5$  was suitable for use in polarization as well. This behaviour of  $\lambda$  can be understood by comparing profiles through sources embedded within images of total intensity and  $L_{\text{RM}}$ , as presented by Hales et al. (2012). They show that above  $T_f = 4$ , Gaussian sources embedded within these two environments are very similar in morphology, modulo statistical fluctuations. For this reason, the relevant cross-sectional area for the peak bias correction,  $H_\lambda$  in equation (13), may be obtained for images of  $L_{\text{RM}}$  using the same value of  $\lambda$  as was recommended for total intensity. Using this value, we found that integrated SB recovery was optimized when flooding down to  $T_f = 4.0$ , as discussed earlier in Section 2.4.2.

In Fig. 9 we present the results of our simulations, where we have executed *IMFIT* using unconstrained Gaussian fit parameters with a  $4\sigma_{\text{RM}}$  cut-off fitting threshold (the same as  $T_f$ ). The results obtained from the same simulations by executing *IMFIT* with constrained point source fits are presented in Fig. 10.

The strong systematic biases exhibited by *IMFIT* in Fig. 9 suggest that its unconstrained fits are unsuited to the statistical environment of  $L_{\text{RM}}$ . We attribute this to a breakdown in the assumption that

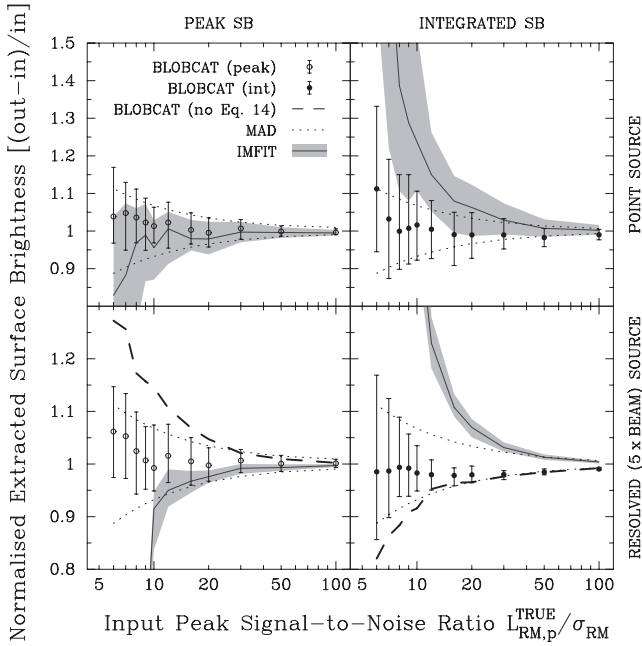


**Figure 9.** SB measurement performance of BLOBCAT in linear polarization,  $L_{RM}$ ; the display layout is duplicated from Fig. 6. Fit parameters for IMFIT are unconstrained. No corrections for polarization bias have been applied.

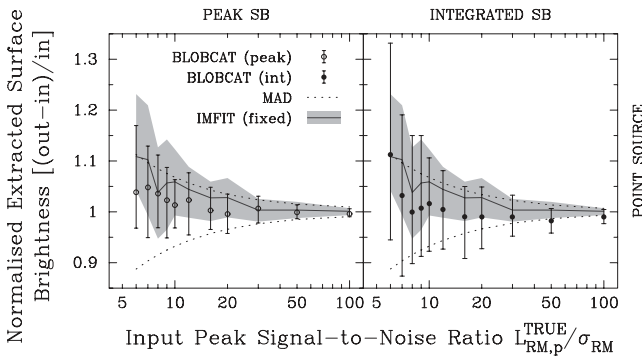


**Figure 10.** Reproduction of the top row of Fig. 9, but here displaying IMFIT results for point source fits with angular dimensions fixed to the image resolution.

sources are superposed with Gaussian noise fluctuations, as required to perform robust least-squares minimization. When IMFIT’s angular size parameters are fixed to the image resolution, the systematic biases in measured SB for input point sources are diminished, as shown in Fig. 10. Through further experimentation, we found that systematic IMFIT biases were unavoidable for all but the most manual, uniquely constrained fits. Reduction or removal of the  $4\sigma_{RM}$  cut-off threshold, used to prevent faint pixels from entering the Gaussian fitting process, was found to worsen systematic trends. We found similar biases to those described above when using IMFIT in images of standard linear polarization,  $L$ .

In contrast, the results from Fig. 9 indicate that BLOBCAT’s measurements of peak and integrated SB are, in effect, systematically unbiased. We justify this claim as follows, beginning with peak SB performance.

The small systematic positive bias exhibited by the recovered peak SB is due to the positive semidefinite nature of  $L_{RM} \geq 0$ ; this effect, which is extrinsic to BLOBCAT, is known as polarization bias.

Because of the intimate relationship that exists between polarization bias and the specifics of observational set-up, as elucidated shortly, BLOBCAT makes no attempt to correct for this bias. To illustrate the variety and complexity of schemes that may be applicable to different data, we note that corrections designed for  $L$  (see Leahy & Fernini 1989) are not suitable for  $L_{RM}$  because they are governed by different statistical distributions (Hales et al. 2012). Furthermore, no fixed (unparametrized) correction scheme<sup>7</sup> is suitable for  $L_{RM}$  because the statistical properties of  $L_{RM}$  are dependent on the underlying observational characteristics of the data such as frequency coverage and channel width (Hales et al. 2012). Instead, more computationally expensive schemes to correct for polarization bias, and potentially Eddington bias (which affects the measured SB of unresolved sources; Eddington 1913), may be required (Hales et al., in preparation). To alleviate polarization bias in BLOBCAT’s measurements of peak SB, users must independently apply their own suitably selected correction scheme.

BLOBCAT appears to accurately recover measurements of integrated SB for unresolved sources, apart from a positive bias exhibited at low input S/N. This latter behaviour is due to polarization bias, which affects sources whose pixel magnitudes are predominantly at low S/N. However, this bias is not of significant consequence because, on average for these sources, their ratios of integrated to peak SB will not deviate significantly from 1. In these cases, their peak values will best represent their flux densities (cf. Section 3.1.2; also Section 4.1), which need only be corrected for polarization bias in order to deliver systematically unbiased measurements.

Turning to BLOBCAT’s measurements of integrated SB for highly resolved sources, their unbiased nature appears to be due to the fortuitous cancellation of two systematic effects. The first of these is the negative bias for resolved sources, as seen earlier for total intensity (the lower right-hand panel of Fig. 6). The second is the positive polarization bias discussed above. We conjecture that the cancellation of these two effects is robust, regardless of the observational set-up dictating the specific statistical description displayed by the input  $L_{RM}$  (or  $L$ ) image. Our justification for this assertion is that the dominant statistical differences between images of  $L_{RM}$  for different observational set-ups, or between images of  $L_{RM}$  and  $L$ , occur below a threshold of  $4\sigma_{RM}$  (Hales et al. 2012). Given that BLOBCAT ignores data below this cut-off threshold (for our recommended  $T_f = 4.0$ ), we are confident that any systematic blob-extraction differences between these images will be below the noise level.

Regarding SB measurement uncertainties, we mirror the earlier discussion of total intensity uncertainties from Section 3.1.2. We note that equations (30) and (32) suitably reflect BLOBCAT’s measurement errors in linear polarization, as exhibited by the dotted lines in Fig. 9. We therefore leave these equations unchanged for use in linear polarization analysis.

### 3.2.3 Results and discussion: position measurements

In Fig. 11, we compare the accuracy of position measurements using both BLOBCAT and IMFIT in recovering the true input positions for our simulated unresolved and resolved sources. As with SB measurements (Section 3.2.2), we find that unconstrained Gaussian fitting

<sup>7</sup> We note that George, Stil & Keller (2011) recently proposed a fixed correction scheme for  $L_{RM}$ . As their scheme implicitly assumes a specific observational set-up, its applicable parameter space is limited.

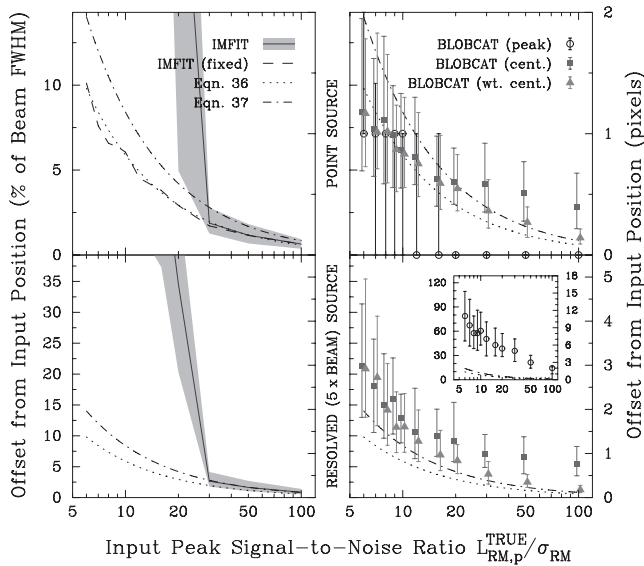


**Figure 11.** Positional accuracy of BLOBCAT and IMFIT in linear polarization,  $L_{RM}$ ; the display layout is duplicated from Fig. 8.

is not appropriate for determining source positions in linear polarization. Following from the discussion for positional measurements in total intensity (Section 3.1.3), we note that BLOBCAT’s weighted centroid positions are also suitable for use in linear polarization, as are the uncertainty estimates using equations (21) and (24).

### 3.3 Complex blobs

In this section, we qualitatively discuss BLOBCAT’s performance when analysing blobs that exhibit complex (resolved, non-Gaussian) morphology. We do not seek to quantitatively address this performance due to the lack of clear standardized test sources. Possible examples of complex blobs include supernova remnant shells, extended lobes of radio galaxies, radio relics and extended Galactic emission; we discuss how these blobs may be automatically identified and flagged for follow-up using BLOBCAT in Section 4. Other examples include blended blobs that consist of multiple overlapped individual Gaussians; we discuss these in Section 4.2.

For each detected blob, BLOBCAT assumes 2D elliptical Gaussian morphology (Section 2.3) so as to infer a debiased peak SB and a corrected integrated SB (Section 2.4). If a detected blob is not of true Gaussian morphology, then its debiased peak SB is unlikely to be significantly affected. This is because the use of  $\lambda = 3.5$  in calculating the relevant cross-sectional area susceptible to peak bias (using equation 14) is still likely to be a suitable choice for non-Gaussian blobs. It is more difficult to generalize the systematic manner in which measurements of corrected integrated SB may differ from their true values. The simplest observation is that low-S/N blobs are more vulnerable than high-S/N blobs to systematic error in their measurements of corrected integrated SB (cf. equation 17). However, the fraction of blob volume remaining unflooded below  $T_f$  will be small for a low-S/N blob that is highly resolved, suggesting that in general, uncorrected integrated SB measurements will be more accurate than corrected integrated SB measurements in estimating flux densities for a majority of complex blobs. We have verified the general statements above by testing BLOBCAT’s performance in handling sources with a range of complex morphologies. We find that BLOBCAT’s performance for slightly extended non-Gaussian blobs that consist of blended Gaussian components, where the approxi-

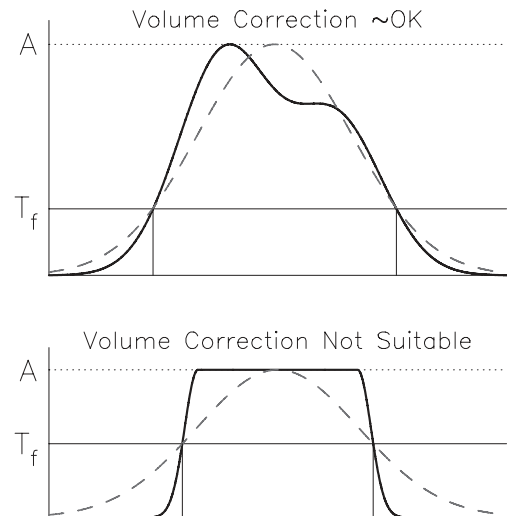


**Figure 12.** When confronted with a non-Gaussian blob (two arbitrary resolved samples illustrated; solid curves), BLOBCAT assumes an idealized Gaussian morphology (dashed curves at equal peak S/N,  $A$ ) so as to infer the fractional volume remaining unflooded below the cut-off threshold ( $T_f$ ). If this assumption is particularly poor, as suggested by the example in the lower panel, then the resulting measurement of volume-corrected integrated SB (using equation 17) may become systematically biased away from the blob’s true flux density. For such blobs, the uncorrected measurement of integrated SB is likely to act as a less-biased estimator of true flux density.

mation of 2D elliptical Gaussian morphology is poor, is in general poorer than the simulation results presented earlier for pathologically resolved Gaussian blobs. However, alternatives for handling such blobs more suitably in post-processing are available, as discussed in Section 4.2. For highly extended non-Gaussian blobs, BLOBCAT’s measurements of uncorrected integrated SB are in general quite accurate because the fraction of unflooded blob volume is always very small.

In Fig. 12, we present two sample non-Gaussian blobs in an attempt to illustrate their potential for integrated SB error. Users should judge for themselves whether corrected ( $S_{int}$ ) or uncorrected ( $S_{int}^{OBS}$ ) measurements of integrated SB best describe the flux densities of their complex blobs; to assist with this decision, BLOBCAT reports both values in its output catalogue. If the two values differ by more than a few per cent, then the corrected values may be unsuitable, and manual inspection is recommended.

Similarly, users should determine which BLOBCAT position measurement is most appropriate for each of their complex blobs; the S/N-weighted centroid may be inappropriate for some blobs. For example, the weighted centroid position for an arc-shaped radio relic (i.e. a crescent moon shape) may be situated beyond the boundaries of its flooded pixels; the raw peak pixel or area (unweighted) centroid position may be more appropriate. To aid users, BLOBCAT catalogues all three position measurements. In addition, flags are produced (see Section 2.6) so as to indicate whether the centroid positions are situated within or exterior to the flooded pixel confines of each blob.

## 4 POST-PROCESSING

BLOBCAT is designed to produce an output catalogue that details basic properties of blobs in an image. Depending on the nature of the data and the requirements of the user, additional processing may be required to make full use of the catalogue.

In this section, we highlight two such examples of post-processing. We first consider a selection procedure for determining which SB measurement (peak or integrated) best describes the flux density of a blob. We then consider a procedure for identifying and analysing blobs that exhibit non-Gaussian morphologies.

#### 4.1 Blob flux densities

The choice of whether to represent a blob's flux density by its measured peak or integrated SB is equivalent to asking whether the blob is unresolved or not. If it is unresolved then the peak SB should be used (explained as follows; note also Appendix A), while for resolved blobs it is the integrated SB that should be used.

The user is responsible for selecting which of the measurements of peak or integrated SB best represent the true flux density for each detected blob. We do not automate this process for the same reason that Gaussian fitting tasks such as `IMFIT` do not, namely that noise features adjacent to faint, unresolved sources may render integrated SB measurements less likely to represent true flux densities than peak SB measurements.

If a user is only interested in a small number of blobs, then as with `IMFIT`, more attention can be paid to each individual fit so as to minimize potential fitting errors, for example through fitting constraints in `IMFIT` or perhaps suitable pixel masking prior to running `BLOBCAT`. For such carefully fitted blobs, their integrated SB measurements may be used to represent their true flux densities, even if they are faint or unresolved. However, for large sample sizes (e.g. for a survey), it is impractical to consider implementation of such manual, or perhaps even machine-learning enabled, fitting procedures. Indeed, attempting to manually fit each source in a survey may inadvertently bias the resulting flux density measurements due to subjectivity on behalf of the user.

Instead, a more appropriate strategy may be initiated by taking the ratio between integrated to peak SB measurements for each blob, so as to characterize the global variance in this ratio as a function of measured S/N. By considering the parameter space populated by noise-affected blobs with  $S_{\text{int}} < S_p$ , an envelope can be designed as a function of S/N to select which of the blobs with  $S_{\text{int}} > S_p$  are likely to be similarly affected by noise. Only those blobs with ratios in excess of the envelope criterion may be deemed resolved, and in turn have their flux densities represented by their integrated SB measurements. All other blobs should have their flux densities represented by their peak SB measurements. This strategy has been employed for `IMFIT`-based surveys of total intensity, e.g. Huynh et al. (2005); application to total intensity and linear polarization surveys with `BLOBCAT` will be presented by Hales et al. (in preparation).

If a blob is resolved, then an estimate of its deconvolved size may be obtained directly from its integrated to peak SB ratio (via division of equation 8 by equation 4), namely

$$\frac{S_{\text{int}}}{S_p} = \frac{\psi_r \psi_s}{\Theta_{\text{maj}} \Theta_{\text{min}}}, \quad (38)$$

where the deconvolved angular size can be estimated using the geometric mean as  $\psi_{\text{deconv}} \approx \sqrt{\psi_r \psi_s - \Theta_{\text{maj}} \Theta_{\text{min}}}$ . Again, illustrations of this procedure are available in total intensity using `IMFIT` (Huynh et al. 2005), and will be presented for total intensity and linear polarization with `BLOBCAT` by Hales et al. (in preparation).

#### 4.2 Blob decomposition

`BLOBCAT` assumes that isolated blobs are of Gaussian morphology in order to catalogue their properties. This assumption will work well

for images that are sparsely populated (i.e. not confusion limited) with Gaussian sources. However, if complex blobs are present (cf. Section 3.3) this assumption may not always be suitable, requiring additional processing of the complex objects so as to suitably characterize their properties. Before commenting on this processing, we briefly outline a simple procedure by which complex blobs may be first identified.

In equation (34) we defined the parameter  $R^{\text{EST}}$ , which estimates the size of a detected blob in units of the sky area covered by an unresolved Gaussian blob with the same peak SB. If  $R^{\text{EST}}$  is large, it indicates that a blob is unlikely to be unresolved.

To illustrate how this parameter may be used to identify potentially complex blobs for follow-up, we preview the general processing steps performed by Hales et al. (in preparation) to catalogue sources in radio-wavelength images of total intensity and linear polarization; details of these images are not pertinent to the discussion here, apart from noting that they consist mostly of compact sources (i.e. there are no widespread extended image features). Hales et al. (in preparation) find that a value of  $R^{\text{EST}} > 1.4$  is well suited for automatically flagging complex blobs. Gaussian fits are attempted for each of these flagged complex blobs with `IMFIT` to determine which ones are likely to consist of single or multiple overlapped (blended) Gaussians. This procedure is semi-automated to require only two initial manual inputs to `IMFIT`: the number of potentially overlapped Gaussians, and their cursory positions. We note here that standard digital imaging techniques such as the Laplacian of Gaussian operation (e.g. Sonka et al. 2008) which is implemented within the `AEGEAN` algorithm (Hancock et al. 2012), blob decomposition algorithms such as `CLUMPFIND` (Williams et al. 1994), or the widely used Watershed transform (Roerdink & Meijster 2000), may be well suited to performing this step automatically. Hales et al. (in preparation) preserve the original `BLOBCAT` measurements for those blobs that are best fitted by a single Gaussian. For each blob identified as being blended, they replace its original `BLOBCAT` catalogue entry with multiple `IMFIT` entries for each individual Gaussian component identified. Remaining from this procedure are a small number of extended, non-Gaussian blobs that cannot be adequately refit using `IMFIT` (as identified due to their large fitting residuals; we note here that image artefacts may also be included in this list, though too many artefacts could indicate undervaluation of rms noise estimates). For each of these remaining blobs, Hales et al. (in preparation) preserve the original `BLOBCAT` measurements and perform a final manual inspection to determine which of the integrated SB measurements should be used to represent the blob's flux density (uncorrected or corrected; Section 3.3).

We envisage that the above procedure may be quickly and easily replicated for future surveys. By performing Gaussian fitting for only those blobs that `BLOBCAT` indicates may be complex, it should be possible to robustly and automatically catalogue all but the most non-Gaussian of sources in an image.

## 5 SUMMARY AND CONCLUSIONS

We have described `BLOBCAT`, an algorithm designed to identify and catalogue blobs in a 2D FITS image of Stokes  $I$  intensity or linear polarization ( $L$  or  $L_{\text{RM}}$ ). Utilizing a Gaussian morphology assumption and two key bias corrections, `BLOBCAT` equips its core flood fill algorithm with the tools necessary to perform robust SB measurement.

Written in `PYTHON`, `BLOBCAT` is easy to use and easy to modify. It is well suited to the analysis of large blind surveys, requiring little manual intervention for images sparsely populated with unresolved

and resolved Gaussian sources, and having the ability to account for spatial variations in both image sensitivity and bandwidth smearing. To indicate BLOBCAT's ability to swiftly analyse data, we note that Hales et al. (in preparation) produce a catalogue of  $\sim 1000$  blobs from an image with  $\sim 10\,000 \times 10\,000$  pixel, including the use of equal-sized rms and bandwidth smearing images, in less than 60 s on a standard desktop computer. While source extractors built around Gaussian fitting routines are competitive with BLOBCAT in this raw computing time, though such comparison is implementation dependent, subsequent overheads associated with manual source inspection may be greatly minimized when using the latter. This is because unresolved and resolved Gaussian blobs are automatically and accurately processed by BLOBCAT, requiring only non-Gaussian blobs to be manually addressed.

Accurate estimates of background rms noise are required to ensure robust and accurate operation of BLOBCAT. We described a simple, objective and automated procedure by which these estimates may be obtained, which makes use of local background mesh calculations. We note that this procedure may be used to estimate background rms noise for use with any source extractor, not just BLOBCAT.

We have demonstrated the performance of BLOBCAT through Monte Carlo simulations of unresolved and resolved Gaussian sources. We benchmarked this performance against that of standard Gaussian fitting, finding comparable results in total intensity and vastly superior results in linear polarization. Our simulations indicate that Gaussian fitting is inappropriate for use in linear polarization for all but the most manually constrained of fits. BLOBCAT contains at present the only algorithm capable of robustly cataloguing accurate flux densities for resolved or extended sources in linear polarization, without incurring significant systematic biases.

In closing, we note that BLOBCAT may be suitable for cautious application to image data at non-radio wavelengths, such as optical, provided that the flooding S/N cut-off is set to a value high enough to avoid measurement systematics induced by low-S/N statistics. Optical pixel shot noise (the Poisson regime) is non-Gaussian at low S/N and limits to Gaussianity at higher S/N, much like the statistics of linear polarization that can be accommodated by BLOBCAT. Modification of BLOBCAT's algorithms may be required to account for wavelength- and instrument-specific descriptions of point spread functions and pixellation errors.

The BLOBCAT program, supplemented with test data to illustrate its use, is available electronically through the World Wide Web at <http://blobcat.sourceforge.net/>.

## ACKNOWLEDGMENTS

We thank the following for helpful discussions and feedback: Tim Cornwell, Mark Calabretta, Andrew Hopkins, Elizabeth Mahony, Paul Hancock, Greg Madsen and Jay Banyer. We thank the anonymous referee for helpful comments that led to the improvement of this paper. CAH acknowledges the support of an Australian Post-graduate Award and a CSIRO OCE Scholarship. The Centre for All-sky Astrophysics is an Australian Research Council Centre of Excellence, funded by grant CE11E0090.

## REFERENCES

Bertin E., Arnouts S., 1996, *A&AS*, 117, 393  
 Bondi M. et al., 2003, *A&A*, 403, 857  
 Brentjens M. A., de Bruyn A. G., 2005, *A&A*, 441, 1217  
 Bridle A. H., Greisen E. W., 1994, AIPS Memo No. 87, NRAO, Charlottesville, VA

Bridle A. H., Schwab F. R., 1999, in ASP Conf. Ser. Vol. 180, *Synthesis Imaging in Radio Astronomy II*. Astron. Soc. Pac., San Francisco, p. 371  
 Briggs D. S., 1995, PhD thesis, The New Mexico Institute of Mining and Technology  
 Briggs D. S., Cornwell T. J., 1992, in Worrall D. M., Biemsderfer C., Barnes J., eds, ASP Conf. Ser. Vol. 25. Astron. Soc. Pac., San Francisco, p. 170  
 Calabretta M. R., Greisen E. W., 2002, *A&A*, 395, 1077  
 Condon J. J., 1997, *PASP*, 109, 166  
 Condon J. J., Cotton W. D., Greisen E. W., Yin Q. F., Perley R. A., Taylor G. B., Broderick J. J., 1998, *AJ*, 115, 1693  
 Cornwell T., Fomalont E. B., 1999, in Taylor G., Carilli C. L., Perley R. A., eds, ASP Conf. Ser. Vol. 180, *Synthesis Imaging in Radio Astronomy II*. Astron. Soc. Pac., San Francisco, p. 187  
 David H. A., Nagaraja H. N., 2003, *Order Statistics*, 3rd edn. Wiley, NJ  
 Deboer D. R. et al., 2009, *Proc. IEEE*, 97, 1507  
 Eddington A. S., 1913, *MNRAS*, 73, 359  
 Ellingson S. W., Clarke T. E., Cohen A., Craig J., Kassim N. E., Pihlstrom Y., Rickard L. J., Taylor G. B., 2009, *Proc. IEEE*, 97, 1421  
 Fishkin K. P., Barsky B. A., 1985, in Magnenat-Thalmann N., Thalmann D., eds, *Proc. Graphics Interface '85*. Springer-Verlag, Tokyo, p. 56  
 Fruchter A. S., Hook R. N., 2002, *PASP*, 114, 144  
 Gaensler B. M., Landecker T. L., Taylor A. R., POSSUM Collaboration, 2010, *BAAS*, 42, 515  
 George S. J., Stil J. M., Keller B. W., 2011, preprint (arXiv:1106.5362)  
 Gooch R., 1996, in Jacoby G. H., Barnes J., eds, ASP Conf. Ser. Vol. 101, *Astronomical Data Analysis Software and Systems V*. Astron. Soc. Pac., San Francisco, p. 80  
 Grant J. K., Taylor A. R., Stil J. M., Landecker T. L., Kothes R., Ransom R. R., Scott D., 2010, *ApJ*, 714, 1689  
 Greisen E. W., 1983, AIPS Memo No. 27, NRAO, Charlottesville, VA  
 Hales C. A., Gaensler B. M., Chatterjee S., van der Swaluw E., Camilo F., 2009, *ApJ*, 706, 1316  
 Hales C. A., Gaensler B. M., Norris R. P., Middelberg E., 2012, *MNRAS*, in press  
 Hancock P. J., Murphy T., Gaensler B. M., Hopkins A., Curran J. R., 2012, *MNRAS*, 422, 1812  
 Heald G., Braun R., Edmonds R., 2009, *A&A*, 503, 409  
 Hills R. E., Kurz R. J., Peck A. B., 2010, *Proc. SPIE*, 7733, 773317  
 Holwerda B. W., 2005, preprint (arXiv:astro-ph/0512139)  
 Hopkins A. M., Afonso J., Chan B., Cram L. E., Georgakakis A., Mobasher B., 2003, *AJ*, 125, 465  
 Huynh M. T., Jackson C. A., Norris R. P., Prandoni I., 2005, *AJ*, 130, 1373  
 Ibar E., Ivison R. J., Biggs A. D., Lal D. V., Best P. N., Green D. A., 2009, *MNRAS*, 397, 281  
 Johnson N. L., Kotz S., 1970, *Distributions in Statistics: Continuous Univariate Distributions – I*. Houghton Mifflin, NY  
 Johnston S. et al., 2008, *Exp. Astron.*, 22, 151  
 Jonas J. L., 2009, *Proc. IEEE*, 97, 1522  
 Joye W. A., Mandel E., 2003, in Payne M. E., Jedreowski R. I., Mook R. N., eds, ASP Conf. Ser. Vol. 295, *Astronomical Data Analysis Software and Systems XII*. Astron. Soc. Pac., San Francisco, p. 489  
 Leahy P., Fernini I., 1989, VLA Scientific Memo No. 161, NRAO, Charlottesville, VA  
 Lieberman H., 1978, in Mauch T., Murphy T., Buttery H. J., Curran J., Hunstead R. W., Piestrzybaski B., Robertson J. G., Sadler E. M., eds, *SIGGRAPH '78 Proceedings*. ACM, New York, p. 111  
 Mauch T. et al., 2003, *MNRAS*, 342, 1117  
 Murphy T., Mauch T., Green A., Hunstead R. W., Piestrzynska B., Kels A. P., Sztajer P., 2007, *MNRAS*, 382, 382  
 Norris R. P. et al., 2006, *AJ*, 132, 2409  
 Norris R. P. et al., 2011, *Publ. Astron. Soc. Australia*, 28, 215  
 Opperman et al., 2012, *A&A*, 542, A93  
 Oosterloo T., Verheijen M. A. W., van Cappellen W., Bakker L., Heald G., Ivashina M., 2009, *PoS (SKADS2009)*, *PoS (IX EVN Symposium)*, 107, 070  
 Oppermann N., Robbers G., Ensslin T. A., 2011, preprint (arXiv:1107.2384)



- O'Sullivan S., Stil J., Taylor A. R., Ricci R., Grant J. K., Shorten K., 2008, in POS, Proc. 9th Eur. VLBI Network Symp. for Radio Astron., p. 107
- Pach J., Agarwal P. K., 1995, *Combinatorial Geometry*. Wiley, New York
- Pence W. D., Chiappetti L., Page C. G., Shaw R. A., Stobie E., 2010, *A&A*, 524, A42
- Perley R. A., Chandler C. J., Butler B. J., Wrobel J. M., 2011, *ApJ*, 739, L1
- Rayleigh J. W. S., 1880, *Philos. Magazine*, 10, 73
- Roerdink J. B. T. M., Meijster A., 2000, *Fundam. Inf.*, 41, 187
- Rottgering H. et al., 2010, *PoS (ISKAF2010)*, 050
- Rudnick L., 2002, *PASP*, 114, 427
- Rudnick L., Brown S., 2009, *AJ*, 137, 145
- Sault R. J., Teuben P. J., Wright M. C. H., 1995, in Shaw R. A., Payne M. E., Hayes J. J. E., eds, *ASP Conf. Ser. Vol. 77, Astronomical Data Analysis Software and Systems IV*. Astron. Soc. Pac., San Francisco, p. 433
- Shi H., Liang H., Han J. L., Hunstead R. W., 2010, *MNRAS*, 409, 821
- Sonka M., Hlavac V., Boyle R., 2008, *Image Processing, Analysis, and Machine Vision*, 3rd edn. Thompson Learning, Toronto
- Subrahmanyan R., Ekers R. D., Saripalli L., Sadler E. M., 2010, *MNRAS*, 402, 2792
- Taylor A. R., Salter C. J., 2010, in Kothes R., Landecker T. L., Willis A. G., eds, *ASP Conf. Ser. Vol. 438, The Dynamic Interstellar Medium: A Celebration of the Canadian Galactic Plane Survey*. Astron. Soc. Pac., San Francisco, p. 402
- Taylor A. R. et al., 2007, *ApJ*, 666, 201
- Tukey J. W., 1977, *Exploratory Data Analysis*. Addison-Wesley, Reading, MA
- Vaillancourt J. E., 2006, *PASP*, 118, 1340
- Williams J. P., de Geus E. J., Blitz L., 1994, *ApJ*, 428, 693; see also <http://www.ifa.hawaii.edu/users/jpw/clumpfind.shtml>
- Wooten A., Thompson A. R., 2009, *Proc. IEEE*, 97, 1463

## APPENDIX A: PIXELLATION ERROR

In radio synthesis imaging, the number of pixels per resolution element (synthesized beam) can be adjusted after the original observations have been made. This is because raw data are obtained in the Fourier plane, enabling post facto oversampling of data in the image plane. By comparison, optical observations are often under-sampled in the image plane, requiring ingenious methods to utilize their full resolution (e.g. the Drizzle algorithm by Fruchter & Hook 2002).

In this appendix, we present implications for SB measurements when sampling a radio image with insufficient pixels. We use the term ‘pixellation error’ to refer specifically to the systematic undervaluation of peak SB measurements due to imaging and fitting effects. We focus on the pixellation error exhibited by two methods of peak SB measurement for unresolved sources. We first derive a relationship for the pixellation error exhibited by measurements of observed (raw) peak SB. We then compare this peak pixel error to that exhibited by the fitted peak of a 2D parabola, where the fit is obtained using a  $3 \times 3$  pixel array about the raw peak pixel (e.g. as implemented in the MIRIAD task MAXFIT). We conclude by commenting on the manner in which image pixellation affects measurements of integrated SB.

In conventional radio synthesis imaging, the sky is assumed to be represented by delta functions; each image pixel is thus a spot sample, as opposed to other sky representations such as piecewise-constant pixels, which require integrals over regions to be computed. To represent the visibility data, sources in images deconvolved using the iterative CLEAN algorithm will be of the form (Briggs & Cornwell 1992; Briggs 1995)

$$S^{\text{OBS}}(x, y) = [\text{BF} * \text{SRC} * \text{BEAM}](x, y), \quad (\text{A1})$$

where  $S^{\text{OBS}}(x, y)$  is the observed source SB distribution at pixel coordinate  $(x, y)$ , the asterisks indicate convolution, BF is a basis

function that depends on whether the source is centred directly on a pixel or not, SRC represents the clean component model of the source and BEAM is the restoring beam. We assume that BEAM is Gaussian.

We define  $\varepsilon^{\text{OBS}} = S_p^{\text{OBS}}/S_p^{\text{TRUE}}$  as the fraction of true peak SB observed within the peak pixel of an unresolved source. We assume  $N_\alpha$  and  $N_\delta$  pixel per projected resolution element such that a pixel dimension is  $\Theta_\alpha/N_\alpha \times \Theta_\delta/N_\delta$ ; here,  $\Theta_\alpha$  and  $\Theta_\delta$  are the major and minor FWHMs that characterize the image resolution (see introductory remark in Section 2.3), as projected along the RA and Dec. axes of an image (see equations 20 and 25).

When the true peak for an unresolved 2D elliptical Gaussian is centred directly on a pixel, which we denote the ‘on-pixel’ case, both the BF and SRC terms in equation (A1) are given by delta functions. The source SB distribution is therefore described by an unattenuated 2D elliptical Gaussian with  $\varepsilon_{\text{on-pixel}}^{\text{OBS}} = 1$ , regardless of the values of  $N_\alpha$  and  $N_\delta$ .

When the true peak is centred halfway between pixel centres, which we denote the ‘off-pixel’ case, SRC is again a delta function (representing a point source) and BEAM is a Gaussian, but now BF must consist of a sinc function in order to represent the visibility data for a shifted delta function. We find that  $\varepsilon_{\text{off-centre}}^{\text{OBS}}$  is therefore given by

$$\begin{aligned} \varepsilon_{\text{off-centre}}^{\text{OBS}} = & \frac{1}{S_p^{\text{TRUE}}} \int_{-\infty}^{\infty} \int_{-\infty}^{\infty} \frac{\sin(\pi l)}{\pi l} \frac{\sin(\pi m)}{\pi m} \\ & \times S_p^{\text{TRUE}} \exp \left\{ -4 \ln [2] \left[ \frac{(x_{1/2} - l)^2}{N_\alpha^2} \right. \right. \\ & \left. \left. + \frac{(y_{1/2} - m)^2}{N_\delta^2} \right] \right\} dl dm, \end{aligned} \quad (\text{A2})$$

evaluated at  $x_{1/2} = y_{1/2} = 0.5$ .

In Fig. A1, we display  $\varepsilon^{\text{OBS}}$  for the on- and off-pixel cases from above; to conform with visual expectations, in the upper panel we plot 1D source profiles and their corresponding 1D pixel values by using a simplified 1D version of equation (A2) (for which only one integral is required). When the underlying true peak for an unresolved source is centred (in 2D) part-way between the on- and off-pixel cases,  $\varepsilon^{\text{OBS}}$  is given by a value between these two solutions, as illustrated by the shading in the lower panel of Fig. A1. We note that the effect of the sinc function in our off-pixel analysis is essentially negligible, only affecting the plotted curves closer to  $\sim 1$  pixel per FWHM. Nevertheless, we have included the calculation for completeness.

In principle, the pixellation error exhibited by measurements of observed peak SB ( $\varepsilon^{\text{OBS}}$ ) may be minimized by imaging with a large number of pixels per resolution element. However, in practice, limited computing resources will often prevent the production or subsequent analysis of such heavily sampled images. Rather than increasing the image sampling  $N_\alpha$  and  $N_\delta$ , the accuracy of peak SB measurements may be increased by performing a fit to the peak value using a 2D parabola; we denote these fitted peak measurements  $S_p^{\text{FIT}}$ . To demonstrate this increased accuracy, in Fig. A1 we illustrate the pixellation error exhibited by 2D parabolic fitting, which we define as  $\varepsilon^{\text{FIT}} = S_p^{\text{FIT}}/S_p^{\text{TRUE}}$ . We note that our  $\varepsilon_{\text{on-pixel}}^{\text{FIT}}$  and  $\varepsilon_{\text{off-pixel}}^{\text{FIT}}$  curves in Fig. A1 were obtained analytically; for brevity, we will not reproduce the straightforward derivation of  $S_p^{\text{FIT}}$  here. This derivation involves evaluating raw pixel intensities from either spot samples from a 2D Gaussian for the on-pixel case, or evaluating equation (A2) at different pixel positions for the off-pixel case, then

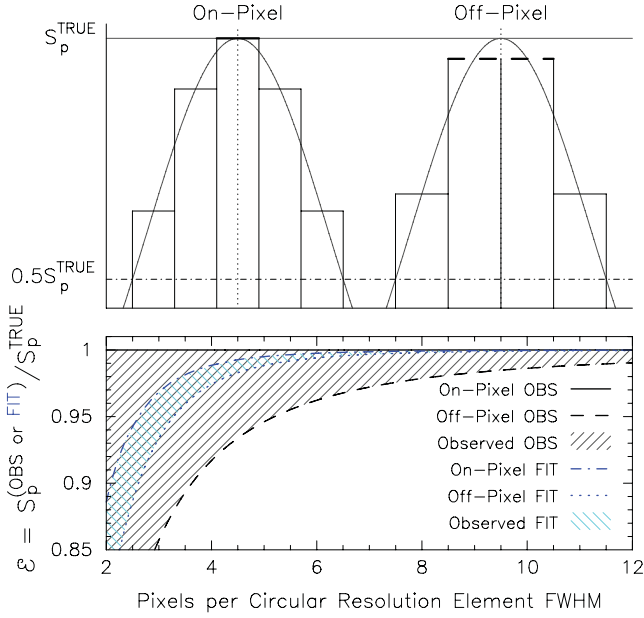


**Figure A1.** Peak SB underestimation due to pixellation; we term this pixellation error. Shown in the upper panel are two unresolved 1D Gaussians with true peak brightness  $S_p^{\text{TRUE}}$ , sampled with 5 (left) and 4 (right) pixel per FWHM. Their true peaks are centred directly on (left) or halfway between (right) pixels. The observed central peak pixel(s) underestimates the true peak brightness of an unresolved 2D elliptical Gaussian by  $\epsilon^{\text{OBS}}$ , as illustrated in the lower panel for the best case (true peak centred on a 2D pixel; solid curve), worst case (true peak placed at the intersection of 4 pixel; dashed curve) and intermediate-case (right-slant shaded) pixellation of a circular resolution element (i.e. assuming  $N_\alpha = N_\delta$ ). Similarly, the underestimation exhibited by the fitted peak of a 2D parabola,  $\epsilon^{\text{FIT}}$ , is illustrated in the lower panel for the best case (dot-dashed curve), worst case (dotted curve) and intermediate-case (left-slant shaded) pixellation scenarios.

performing least squares to solve for an overdetermined system of linear equations (six unknown fit parameters and nine constraining pixels).

Both  $S_p^{\text{OBS}}$  and  $S_p^{\text{FIT}}$  exhibit pixellation error; the latter measure of peak SB is more accurate. To limit pixellation error to within 1 per cent using  $S_p^{\text{OBS}}$ , at least 12 pixel per FWHM are required; for  $S_p^{\text{FIT}}$ , this number falls to around 5. We suggest that observers estimate the degree to which their peak SB measurements may be in error due to pixellation and incorporate this into their error budgets. In BLOBCAT, which catalogues fitted peak SB values ( $S_p^{\text{FIT}}$ ), this is implemented using a pixellation error parameter which we define as  $\Delta S_p^{\text{PIX}} = (1 - \epsilon_{\text{off-centre}}^{\text{FIT}})$ ; this parameter is applied in equation (30). We note that the inclusion of this parameter will tend to (slightly) overestimate peak SB errors for resolved sources; we see this as more appropriate than underestimating peak SB errors for point sources because this error is unlikely to be relevant for resolved sources (where the integrated SB represents the flux density; see Section 4.1).

Finally, we note that integrated SB measurements are less affected by pixellation error than peak pixels. This is because integrated SB is conserved when summing over multiple pixels. This conservation is limited only by noise fluctuations and the ratio between the peak S/N of a source and the flood fill cut-off. To illustrate this limitation, consider a faint unresolved source situated in a heavily pixellated image (i.e. where  $N_\alpha$  and  $N_\delta$  are small). The profile of this source will be poorly mapped by the pixels, rendering BLOBCAT's integrated SB measurement (via equation 16) vulnerable to negative bias.

However, in general this vulnerability will not be an issue because it is the peak SB that is the important value for unresolved sources (see Section 4.1).

## APPENDIX B: BLOBCAT INPUTS

For completeness, a full list of program input arguments to BLOBCAT is presented below. Note that not all arguments may be required for analysis (see Sections 2.5 and 2.6; see also the default values provided in the code). For example, if errors are not required (or are not suitably defined for a particular observational scenario), the input arguments relating to errors below may be ignored. (Conversely, new input arguments may be easily defined by the user and incorporated into BLOBCAT.)

### Argument 1: SB\_image.fits

FITS image of SB in Stokes  $I$  intensity (or Stokes  $Q$ ,  $U$  or  $V$  intensities under limited conditions) or linear polarization ( $L$  or  $L_{\text{RM}}$ ); see Section 2.1.1.

### Argument 2: rmsval

Uniform (spatially invariant) background rms noise level within SB image. This is required if Argument 3 is not provided.

### Argument 3: rmsmap

FITS image of background rms noise; see Section 2.1.2.

### Argument 4: bwsva1

Uniform (spatially invariant) level of bandwidth smearing present in the SB image. This is required if Argument 5 is not provided. To ignore bandwidth smearing, this value should be set to 1.

### Argument 5: bwsmap

FITS image of background rms noise; see Section 2.1.3.

### Arguments 6–8: bmaj, bmin, bpa

Image resolution (beam) parameters; these are only required if image header items are incorrect or incomplete (at present, beam parameters are not standard FITS headers).

### Arguments 9 and 10: dSNR, fSNR

S/N thresholds for blob detection ( $T_d$ ) and flooding cut-off ( $T_f$ ); see Section 2.2.

### Argument 11: pmep

Maximum estimated peak SB attenuation due to pixellation error (see Appendix A); defined here as the maximum anticipated value of  $(1 - \epsilon_{\text{off-centre}}^{\text{FIT}})$ . When set to a value greater than 0, this parameter will ensure that sources with raw observed peak SB less than the nominated detection threshold ( $S_p^{\text{OBS}} < T_d$ ), yet fitted peak SB greater than this threshold ( $S_p^{\text{FIT}} \geq T_d$ ), will be accepted into the catalogue. If ignored, pmep will default to 1, causing BLOBCAT to check all blobs with  $S_p^{\text{OBS}} \geq T_f$  for catalogue acceptance (though this will increase BLOBCAT's run-time, particularly if  $T_d$  and  $T_f$  differ greatly in magnitude).

### Arguments 12 and 13: cpeRA, cpeDec

Phase calibrator positional error in RA ( $\sigma_{\alpha, \text{cal}}$ ) and Dec. ( $\sigma_{\delta, \text{cal}}$ ); see Section 2.6.

### Argument 14: SEM

Standard error of the mean of the variation in the phase corrections resulting from phase self-calibration ( $\sigma_{\text{SEM}}$ ), which is used to calculate  $\sigma_{\text{frame}}$ ; see Section 2.6.

### Argument 15: pasbe

Percentage absolute SB error resulting from calibration ( $\Delta S^{\text{ABS}}$ ); see Section 2.6.

### Argument 16: pppe

Percentage peak SB pixellation error ( $\Delta S^{\text{PIX}}$ ); see Section 2.6 and Appendix A.

### Argument 17: cb

Average clean bias correction ( $\Delta S^{\text{CB}} \geq 0$ ); see Section 2.6.

*Argument 18:* lamfac

$\lambda$  factor for peak SB bias correction; see Section 2.4.1.

*Argument 19:* visArea

Option to calculate visibility areas (can increase program run-time by more than an order of magnitude); see Section 2.6.

*Arguments 20–22:* minpix, maxpix, pixdim

Minimum and maximum accepted blob sizes in pixels and minimum number of pixels in RA/Dec. dimensions for accepted blobs (useful for filtering out easily identified image artefacts).

*Argument 23:* edgemin

Edge buffer in pixels; if flood fill attempts to enter this buffer zone, the blob is rejected (and reported to the user).

*Arguments 24 and 25:* write, hfill

Options to write flooded blobs to an output FITS file and to set the blob highlight value; see Section 2.7.

*Arguments 26 and 27:* kvis, ds9

Options to write an output kvis or ds9 overlay file; see Section 2.7.

*Arguments 28 and 29:* plot, plotRng

Option to produce a diagnostic screen plot displaying flooded blobs in the SB image, and an additional option to specify this plot's dynamic range.

This paper has been typeset from a  $\text{\TeX/L\AA\TeX}$  file prepared by the author.